

Examining the model dependence of extracting the kinetic freeze-out temperature and transverse flow velocity in small collision system

Hai-Ling Lao¹, Fu-Hu Liu^{1,*}, Bao-Chun Li¹, Mai-Ying Duan¹, Roy A. Lacey²

¹*Institute of Theoretical Physics & State Key Laboratory of Quantum Optics and Quantum Optics Devices, Shanxi University, Taiyuan, Shanxi 030006, China*

²*Departments of Chemistry & Physics, Stony Brook University, Stony Brook, NY 11794, USA*

Abstract: The transverse momentum distributions of identified particles produced in small collision systems at the RHIC and LHC have been analyzed by four models. The first two models utilize the blast-wave model with different statistics. The last two models perform some linear tendencies based on different distributions. The four models describe similarly well the experimental data measured by the PHENIX, STAR, and ALICE Collaborations. It is found that both the kinetic freeze-out temperature and transverse flow velocity in central collisions are comparable with those in peripheral collisions. With the increase of collision energy from the RHIC to LHC, the considered quantities do not decrease in general. Comparing with central collisions, proton-proton collisions are closer to peripheral collisions.

Keywords: kinetic freeze-out temperature, transverse flow velocity, small collision system, central collisions, peripheral collisions

PACS: 25.75.Ag, 25.75.Dw, 24.10.Pa

1 Introduction

As an important concept in both thermal physics and subatomic physics, the temperature is widely used in experimental measurements and theoretical studies. Different from macroscopical thermal physics, the temperature in microscopical subatomic physics can not be measured directly, though the temperature measured in thermal physics is reflected by change of given quantity of thermometric material. Instead, we can calculate the temperature by using the methods of particle ratios and transverse momentum (p_T) spectra. The temperature obtained from particle ratios is usually the chemical freeze-out temperature (T_{ch}) which leads to the description of the excitation degree of the interacting system at the stage of chemical equilibrium. The temperature obtained from p_T spectra with the thermal distribution that does not include flow effect is usually the effective temperature (T_{eff} or T) which is not a real temperature due to its relation to particle mass. The temperature obtained from p_T spectra with the thermal distribution which includes flow effect is usually the kinetic freeze-out temperature (T_{kin} or T_0) which describes the excitation degree of the interacting system at the stage of

kinetic and thermal equilibrium.

The chemical freeze-out and kinetic freeze-out are two main stages of the interacting system evolution in high energy collisions. At the stage of chemical freeze-out, the chemical components (relative fractions) of particles are fixed. At the stage of kinetic freeze-out, p_T and momentum (p) spectra of particles are no longer changed. We are interested in T_0 due to its relation to the p_T spectrum of identified particles which is one of the quantities measured at the “first day” in experiments. At the same time, T_0 is related to the structure of phase diagram in the T_0 -related spaces such as T_0 against β_T , and T_0 against $\sqrt{s_{NN}}$, where β_T denotes the mean transverse flow velocity which is caused by the impact and squeeze, $\sqrt{s_{NN}}$ denotes the center-of-mass energy per nucleon pair in collisions of nuclei [\sqrt{s} in particle collisions such as in proton-proton (p - p or pp) collisions]. In particular, in the energy ranges available in the beam energy scan (BES) program at the Relativistic Heavy Ion Collider (RHIC) and the BES program at the Super Proton Synchrotron (SPS), the chemical potential (μ_B) of baryons has to be considered due to the fact that it is non-negligible. Then, the structure of phase diagram in T_0 against μ_B space can be studied in both the RHIC

*E-mail: fuhuliu@163.com; fuhuliu@sxu.edu.cn

BES and SPS BES energy ranges.

Generally, μ_B can be obtained from the particle ratios and its excitation function is studied in detail [1–5], and T_0 and β_T can be obtained from the p_T spectra. In Refs. [6–13], different methods for the extractions of T_0 and β_T are used. In our recent work [14–17], we have used a few models to extract T_0 and β_T in nucleus-nucleus [gold-gold (Au-Au) and lead-lead (Pb-Pb)] collisions at the RHIC and Large Hadron Collider (LHC) energies, where the top RHIC energy is $\sqrt{s_{NN}} = 200$ GeV and the LHC energy reaches a few TeVs. The similar results are obtained in the case of using non-zero β_T in peripheral nucleus-nucleus collisions in the Blast-Wave model with Boltzmann-Gibbs statistics (the BGBW model) [6–8, 18] and with Tsallis statistics (the TBW model) [9, 18, 19]. Our results show that T_0 (β_T) in central nucleus-nucleus collisions is comparable to that in peripheral collisions. Similarly, T_0 and β_T at the LHC are close to those at the RHIC.

It is interesting to compare the results of different models in small collision systems such as pp and deuteron-gold (d -Au) collisions at the RHIC, and pp and proton-lead (p -Pb) collisions at the LHC. In this paper, we shall use four models to extract T_0 and β_T from the p_T spectra of identified particles produced in pp and d -Au collisions at the RHIC, and in pp and p -Pb collisions at the LHC. The model results on the p_T spectra are compared with each other and with the experimental data of the PHENIX [20], STAR [21–23], and ALICE Collaborations [24–25]. Then, similar T_0 and β_T are extracted from the analyses of experimental data by four models.

The paper is structured as follows. The formalism and method are described in Section 2. Results and discussion are given in Section 3. In Section 4, we summarize our main observations and conclusions.

2 Formalism and method

Four models are used for p_T distributions in the present work for comparisons in small collision systems, though they are used to extract T_0 and β_T in nucleus-nucleus collisions at the RHIC and LHC energies in our recent work [14] by somehow different superposition of soft excitation and hard scattering components. The four models can be found in the references mentioned above. However, in order to give a whole representation of the present work, we show it directly and concisely as follow.

i) The BGBW model [6–8] in which we consider a

non-zero β_T of the produced particles.

According to refs. [6–8], the BGBW model results in the p_T distribution to be

$$f_1(p_T) = \frac{1}{N} \frac{dN}{dp_T} = C_1 p_T m_T \int_0^R r dr \times I_0 \left[\frac{p_T \sinh(\rho)}{T_0} \right] K_1 \left[\frac{m_T \cosh(\rho)}{T_0} \right], \quad (1)$$

where N is the number of particles, C_1 is the normalized constant, I_0 and K_1 are the modified Bessel functions of the first and second kinds, respectively, $m_T = \sqrt{p_T^2 + m_0^2}$ is the transverse mass, $\rho = \tanh^{-1}[\beta(r)]$ is the boost angle, $\beta(r) = \beta_S(r/R)^{n_0}$ is a self-similar flow profile, β_S is the flow velocity on the surface, r/R is the relative radial position in the thermal source [6], and $n_0 = 2$ as used in ref. [6]. There is the relation, $\beta_T = (2/R^2) \int_0^R r \beta(r) dr = 2\beta_S/(n_0 + 2) = 0.5\beta_S$, between β_T and $\beta(r)$.

ii) The TBW model [9] in which non-zero β_T is also considered by us.

According to refs. [9], the TBW model results in the p_T distribution to be

$$f_2(p_T) = \frac{1}{N} \frac{dN}{dp_T} = C_2 p_T m_T \int_{-\pi}^{\pi} d\phi \int_0^R r dr \left\{ 1 + \frac{q-1}{T_0} [m_T \cosh(\rho) - p_T \sinh(\rho) \cos(\phi)] \right\}^{-q/(q-1)}, \quad (2)$$

where C_2 is the normalized constant, q is an entropy index that characterizes the degree of non-equilibrium, ϕ denotes the azimuth [9], and $n_0 = 1$ as used in ref. [9]. In fact, n_0 is insensitive in the first two models. It does not matter if we use $n_0 = 1$ or $n_0 = 2$. To be the same as refs. [6] and [9], we use $n_0 = 2$ in the first model and $n_0 = 1$ in the second model. It should be noted that we use the index $-q/(q-1)$ in Eq. (2) instead of $-1/(q-1)$ in ref. [9] due to the fact that q is very close to 1. This substitution results in a small and negligible difference in the Tsallis distribution [19].

iii) The alternative method in which the intercept in T against m_0 relation is regarded as T_0 [7, 10–13], the slope in $\langle p_T \rangle$ against \overline{m} relation is regarded as β_T , and the slope in $\langle p \rangle$ against \overline{m} relation is regarded as the radial flow velocity β [14–17] which does not include the contribution of longitudinal flow, where m_0 denotes the rest mass, \overline{m} denotes the mean moving mass (mean energy), $\langle \dots \rangle$ denotes the theoretical distribution average of the considered quantity, and T is obtained by the Boltzmann distribution [18].

We need two steps to obtain T_0 and β_T . To use the relations $T = T_0 + am_0$, $\langle p_T \rangle = b_1 + \beta_T \overline{m}$, and

$\langle p \rangle = b_2 + \beta \overline{m}$, where a , b_1 , and b_2 are fitted parameters, we choose the form of Boltzmann distribution [18]

$$f_3(p_T) = \frac{1}{N} \frac{dN}{dp_T} = C_3 p_T m_T \exp\left(-\frac{m_T}{T}\right), \quad (3)$$

where C_3 is the normalized constant related to the free parameter T and particle mass m_0 due to its relation to m_T , though the Boltzmann distribution has multiple forms [18].

iv) The same as the third model, but T is obtained by the Tsallis distribution [18, 19].

We choose the form of Tsallis distribution [18, 19]

$$f_4(p_T) = \frac{1}{N} \frac{dN}{dp_T} = C_4 p_T m_T \left(1 + \frac{q-1}{T} m_T\right)^{-q/(q-1)}, \quad (4)$$

where C_4 is the normalized constant related to the free parameters T and q , as well as m_0 , though the Tsallis distribution has more than one forms [18, 19].

As used in our recent work [14], in both the BGBW and TBW models, a non-zero β_T of the produced particles is considered in peripheral nucleus-nucleus collisions. The peripheral collisions contain a few participant nucleons that take part in the violent interactions. This situation is similar to small collision system which also contains a few participant nucleons. In the case of neglecting the influence of cold nuclear effect, small collision system is much similar to peripheral collisions. This means that a non-zero β_T should be considered for small collision system to keep the consistency, though the values of β_T for small collision system and peripheral collisions are possibly different. Naturally, it is not surprised if the values of β_T in the two types of collisions are nearly the same.

From the first model, one can obtain T_0 and β_T . While from the second model, one can obtain T_0 , β_T , and q . The reason that we should utilize the first two models is to compare the results of the models. Although the forms of the first two models are obviously different, the values of T_0 (β_T) obtained from them have a little difference. The last two models are used due to the same reason. We should also utilize the last two models to compare the results of the models. The obtained values from the last two models have a little difference, though they are obviously different.

The description of all the above models is presented at the mid-rapidity. That is the rapidity $y \approx 0$, where $y \equiv 0.5 \ln[(E + p_z)/(E - p_z)]$, and E and p_z denote the energy and longitudinal momentum, respectively. At high p_T , $y \approx -\ln \tan(\vartheta/2) \equiv \eta$, where ϑ and η de-

note the emission angle and pseudorapidity of considered particle, respectively. The influence of the spin and chemical potential on the p_T spectra is neglected due to small effect at the top RHIC and LHC energies [1–4]. As what we did in our recent work [14], the kinetic freeze-out temperature, the mean transverse (radial) flow velocity, and the effective temperature in different models are uniformly denoted by T_0 , β_T , and T , respectively, though different values can be extracted by different models.

Eqs. (1)–(4) are the functions which describe mainly the contribution of soft excitation process. They are only valid for the spectra in a narrow p_T range which covers mainly from 0 to 2.5–3.5 GeV/ c in most cases or a little more in some cases. Even for the soft excitation process, the Boltzmann distribution is not enough to fit the p_T spectra in some cases. In the case of using two- or three-component Boltzmann distribution, T is the weighted average due to different effective temperatures and corresponding fractions obtained from different components.

Generally, two main processes in high energy collisions are considered in the present work. Except for the soft excitation process, another main process is the hard scattering process which contributes the spectra in a wide p_T range and is described by an inverse power-law

$$f_H(p_T) = \frac{1}{N} \frac{dN}{dp_T} = A p_T \left(1 + \frac{p_T}{p_0}\right)^{-n} \quad (5)$$

according to the quantum chromodynamics (QCD) calculus [26–28], where p_0 and n are free parameters, and A is the normalized constant related to the free parameters. As a result of the QCD-based calculation, Eq. (5) contributes the distribution in a range from 0 to high p_T range. Theoretically, although there are overlapping regions in low p_T range between the contributions of Eqs. (1)–(4) and (5), they cannot replace each other.

The experimental p_T spectra distribute usually in a wide range. This means that we have to use a superposition of both the contributions of soft and hard processes (components) to fit the spectra. We use the usual step function for structuring the superposition in order to avoid the entanglement between the contribution ranges of soft excitation and hard scattering components. That is

$$f_0(p_T) = \frac{1}{N} \frac{dN}{dp_T} = A_1 \theta(p_1 - p_T) f_S(p_T) + A_2 \theta(p_T - p_1) f_H(p_T), \quad (6)$$

where $f_S(p_T)$ denotes one of Eqs. (1)–(4), A_1 and A_2

are the constants which result in the contributions of soft and hard components to be the same at $p_T = p_1$, and the step function $\theta(x) = 1$ if $x > 0$ or $\theta(x) = 0$ if $x < 0$. The contribution fraction (rate) of the soft component is given by $k = \int_0^{p_1} A_1 f_S(p_T) dp_T$. Because of respective ranges of different contributions, the selections of parameters in Eqs. (1)–(4) and (5) have no correlation or influence on each other.

The contribution of resonance production for pions and strong stopping effect for participant nucleons are non-negligible at very low ranges in some cases. We have to use a very-soft component for the p_T range from 0 to 0.5–1.5 GeV/c. Let us consider the contribution of the very-soft component. Then Eq. (6) is revised so that it reads

$$\begin{aligned} f_0(p_T) &= \frac{1}{N} \frac{dN}{dp_T} = A_{VS} \theta(p_{VS} - p_T) f_{VS}(p_T) \\ &+ A_1 \theta(p_T - p_{VS}) \theta(p_1 - p_T) f_S(p_T) \\ &+ A_2 \theta(p_T - p_1) f_H(p_T), \end{aligned} \quad (7)$$

where $f_{VS}(p_T)$ denotes one of Eqs. (1)–(4) as what $f_S(p_T)$ denotes, and A_{VS} is the constant which results in the contributions of very-soft and soft components to be the same at $p_T = p_{VS}$. Let us denote by k_{VS} and k_S the rates of the very-soft and soft components, respectively. We have $k_{VS} = \int_0^{p_{VS}} A_{VS} f_{VS}(p_T) dp_T$ and $k_S = \int_{p_{VS}}^{p_1} A_1 f_S(p_T) dp_T$, where $k_{VS} + k_S = k$ [see the text following Eq. (6) for k].

In Eq. (7), although $f_{VS}(p_T)$ and $f_S(p_T)$ have the same formular form, their contribution ranges are different. At the same time, the contribution range of $f_H(p_T)$ is different from those of $f_{VS}(p_T)$ and $f_S(p_T)$. The three functions have no correlation or influence in the fitting procedure. In fact, we fit $f_{VS}(p_T)$ at very-soft p_T from 0 to 0.5–1.5 GeV/c, fit $f_S(p_T)$ at soft p_T from 0.5–1.5 GeV/c to 2.5–3.5 GeV/c, and fit $f_H(p_T)$ at hard p_T from 2.5–3.5 GeV/c to the maximum. In the case of having no $f_{VS}(p_T)$, Eq. (7) descends to Eq. (6). Then, we fit $f_S(p_T)$ in Eq. (6) from 0 to 2.5–3.5 GeV/c. In the calculation, we use the weighted average of parameters due to their different fractions in very soft and soft components in Eq. (7) in order to compare the obtained values from Eqs. (6) and (7).

3 Results and discussion

In Fig. 1, the transverse momentum spectra, $1/(2\pi p_T) \cdot d^2N/(dy dp_T)$, are shown for (a)–(c) positively charged pions (π^+), positively charged kaons (K^+), and protons (p), as well as for (b)–(d) negatively charged

pions (π^-), negatively charged kaons (K^-), and antiprotons (\bar{p}) produced in (a)–(b) 0–20% and (c)–(d) 60–88% (40–100%) d -Au collisions at $\sqrt{s_{NN}} = 200$ GeV. The closed and open symbols represent the experimental data of the PHENIX and STAR Collaboration measured in the pseudorapidity range $|\eta| < 0.35$ [20] and the rapidity range $|y| < 0.5$ [21], respectively. The curves show the results obtained by models i)–iv). The fit parameters are given in Tables 1–4, respectively. Most of them are fitted by Eq. (6). The numerical values fitted by Eq. (7) are marked by a star at the end of line, in which the results obtained from the very-soft and soft components are combined. The results for the very soft and soft components are not listed separately in order to avoid triviality. One can see that the four considered models describe similarly well the p_T spectra of identified particles produced in central (0–20%) and peripheral (60–88% and 40–100%) d -Au collisions at $\sqrt{s_{NN}} = 200$ GeV.

Figure 2 is the same as Fig. 1, but it shows the spectra of (a) π^+ , K^+ , and p , as well as (b) π^- , K^- , and \bar{p} , produced in pp collisions at $\sqrt{s} = 200$ GeV. The closed and open symbols represent the experimental data of the STAR Collaboration measured in $-0.5 < y < 0$ and $|y| < 0.5$, respectively [22, 23]. The fit parameters are given in Tables 1–4. One can see that the four considered models describe similarly well the p_T spectra of identified particles produced in pp collisions at $\sqrt{s} = 200$ GeV.

Figure 3 is the same as Fig. 1, but it shows the spectra of $\pi^+ + \pi^-$, $K^+ + K^-$, and $p + \bar{p}$ produced in (a) 0–5% and (b) 80–100% p -Pb collisions at $\sqrt{s_{NN}} = 5.02$ TeV. The symbols represent the experimental data of the ALICE Collaboration measured in $-0.5 < y < 0$ [24]. It can be seen in most cases that the four considered models describe similarly well the p_T spectra of identified particles produced in p -Pb collisions at $\sqrt{s_{NN}} = 5.02$ TeV.

Figure 4 is the same as Fig. 1, but it shows the spectra, $(1/N_{EV}) \cdot 1/(2\pi p_T) \cdot d^2N/(dy dp_T)$, of $\pi^+ + \pi^-$, $K^+ + K^-$, and $p + \bar{p}$ produced in pp collisions at $\sqrt{s} = 2.76$ TeV, where N_{EV} denotes the number of events and is usually omitted. The symbols represent the experimental data of the ALICE Collaboration measured in $|y| < 0.5$ for low- p_T particles and in $|\eta| < 0.8$ for high- p_T particles [25]. The four considered models describe similarly well the p_T spectra of the identified particles produced in pp collisions at $\sqrt{s} = 2.76$ TeV can be seen in most cases.

It should be noted that although we have used many

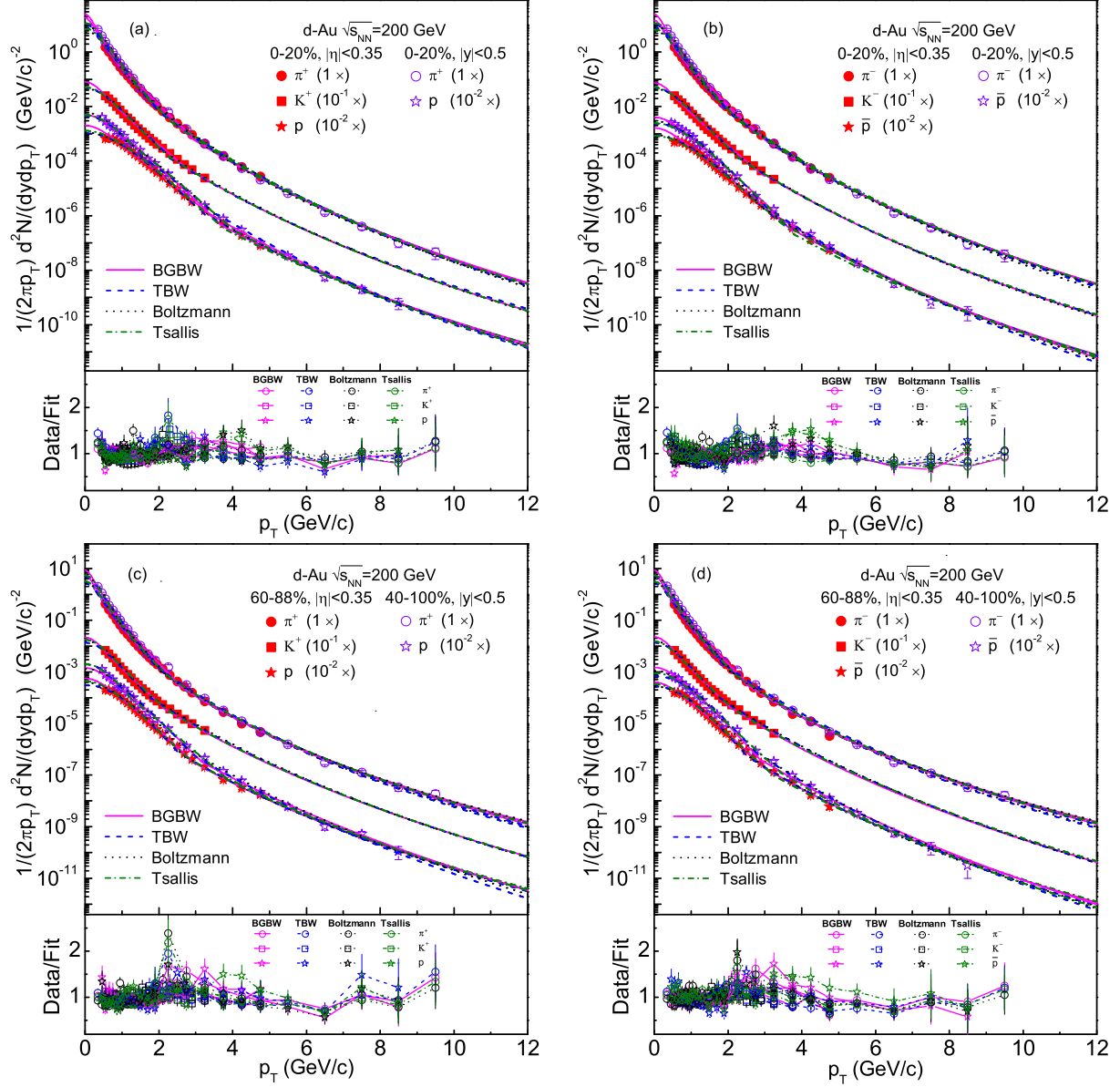


Fig. 1. (Color online) Transverse momentum spectra of (a)-(c) π^+ , K^+ , and p , as well as (b)-(d) π^- , K^- , and \bar{p} produced in (a)-(b) 0–20% and (c)-(d) 60–88% (40–100%) d -Au collisions at $\sqrt{s_{NN}} = 200$ GeV, where the spectra for different particles are multiplied by different amounts shown in the panels for the clarity. The closed and open symbols represent the experimental data of the PHENIX and STAR Collaboration measured in $|\eta| < 0.35$ [20] and $|y| < 0.5$ [21], respectively. The solid, dashed, dotted, and dashed-dotted curves are our results fitted by Eq. (6) or (7) in which $f_S(p_T)$ ($f_{VS}(p_T)$) denote $f_1(p_T)$, $f_2(p_T)$, $f_3(p_T)$, and $f_4(p_T)$, respectively. Bottom panels show the data to fit ratios.

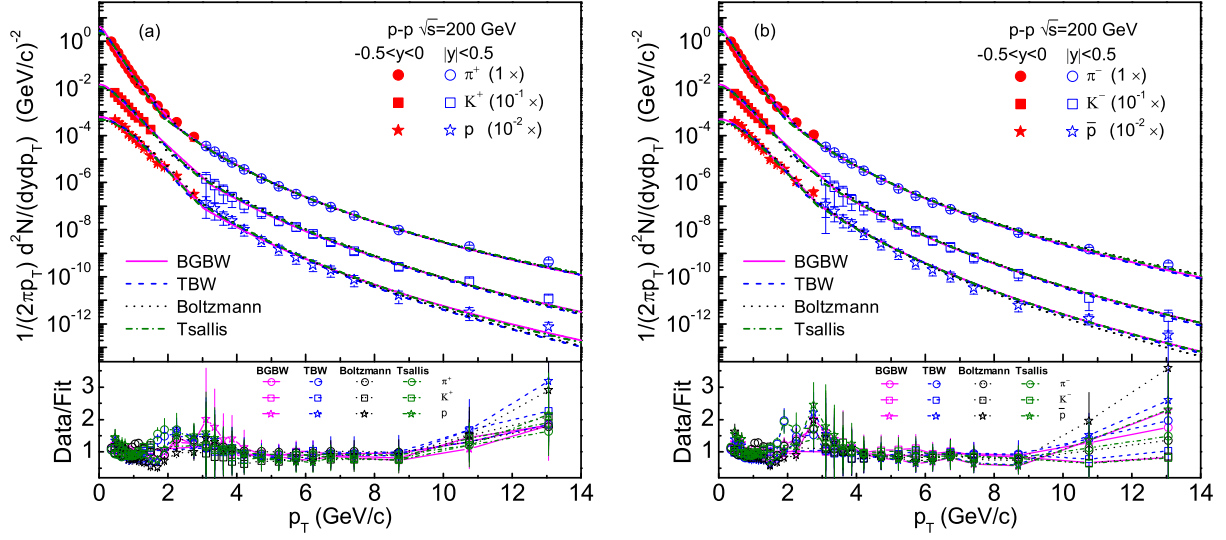


Fig. 2. (Color online) Same as Fig. 1, but showing the spectra of (a) π^+ , K^+ , and p , as well as (b) π^- , K^- , and \bar{p} , produced in pp collisions at $\sqrt{s} = 200$ GeV. The closed and open symbols represent the experimental data of the STAR Collaboration measured in $-0.5 < y < 0$ and $|y| < 0.5$, respectively [22, 23].

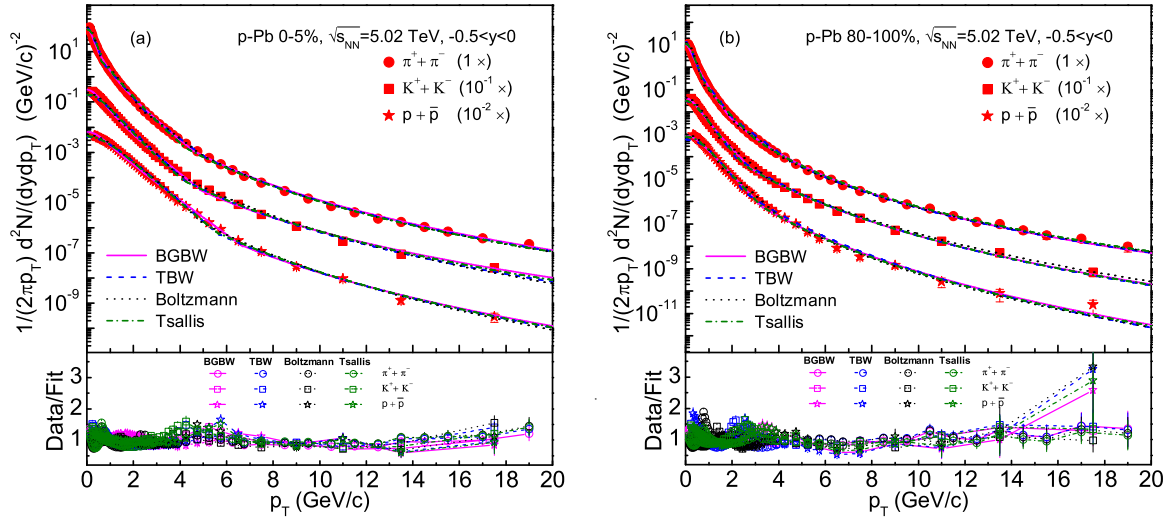


Fig. 3. (Color online) Same as Fig. 1, but showing the spectra of $\pi^+ + \pi^-$, $K^+ + K^-$, and $p + \bar{p}$ produced in (a) 0–5% and (b) 80–100% p -Pb collisions at $\sqrt{s_{NN}} = 5.02$ TeV. The symbols represent the experimental data of the ALICE Collaboration measured in $-0.5 < y < 0$ [24].

Table 1. Values of parameters (T_0 , β_T , k , p_0 , and n), normalization constant (N_0), χ^2 , and dof corresponding to the fits of the BGBW model and inverse power-law [Eqs. (1) and (5) through Eq. (6) or (7)] in Figs. 1–4 and 8. The collision types, data sources, and collisions energies are listed in the blank spaces of the first two columns for the purpose of clarity. The results combined the very-soft and soft components are marked by a star (*) at the end of line.

Figure	Centrality	Particle	T_0 (GeV)	β_T (c)	k	p_0 (GeV/c)	n	N_0	χ^2/dof
1(a)	0–20%	π^+	0.112 ± 0.006	0.43 ± 0.01	0.999 ± 0.001	5.0 ± 0.3	15.9 ± 0.4	4.85 ± 0.51	37/18
<i>d</i> -Au	200 GeV	K^+	0.128 ± 0.008	0.42 ± 0.01	0.994 ± 0.006	5.8 ± 0.3	16.5 ± 0.4	0.64 ± 0.07	9/15
PHENIX		p	0.130 ± 0.008	0.39 ± 0.01	0.998 ± 0.002	5.2 ± 0.3	15.2 ± 0.4	0.30 ± 0.02	64/18
1(b)	0–20%	π^-	0.121 ± 0.006	0.43 ± 0.01	0.999 ± 0.001	5.4 ± 0.3	16.7 ± 0.4	4.30 ± 0.50	23/18
		K^-	0.121 ± 0.008	0.43 ± 0.01	0.995 ± 0.004	6.1 ± 0.3	17.3 ± 0.4	0.60 ± 0.06	7/15
		\bar{p}	0.129 ± 0.008	0.39 ± 0.01	0.999 ± 0.001	5.1 ± 0.2	16.1 ± 0.4	0.24 ± 0.02	103/18
1(c)	60–88%	π^+	0.104 ± 0.006	0.43 ± 0.01	0.998 ± 0.002	3.5 ± 0.2	12.9 ± 0.3	1.29 ± 0.14	30/18
		K^+	0.116 ± 0.008	0.41 ± 0.01	0.982 ± 0.008	6.4 ± 0.2	17.2 ± 0.4	0.15 ± 0.02	12/15
		p	0.119 ± 0.009	0.37 ± 0.01	0.996 ± 0.004	5.5 ± 0.2	15.6 ± 0.3	0.07 ± 0.01	33/18
1(d)	60–88%	π^-	0.104 ± 0.006	0.43 ± 0.01	0.998 ± 0.002	3.5 ± 0.2	12.9 ± 0.3	1.29 ± 0.08	36/18
		K^-	0.115 ± 0.008	0.40 ± 0.01	0.983 ± 0.011	6.0 ± 0.2	17.2 ± 0.3	0.15 ± 0.02	15/15
		\bar{p}	0.119 ± 0.008	0.37 ± 0.01	0.997 ± 0.003	5.5 ± 0.2	16.6 ± 0.3	0.05 ± 0.01	31/18
1(a)	0–20%	π^+	0.111 ± 0.006	0.43 ± 0.01	0.999 ± 0.001	4.4 ± 0.2	15.3 ± 0.3	9.20 ± 0.99	21/18
<i>d</i> -Au	200 GeV	p	0.128 ± 0.008	0.37 ± 0.01	0.998 ± 0.002	5.1 ± 0.2	15.9 ± 0.3	0.97 ± 0.10	18/16
1(b)	0–20%	π^-	0.111 ± 0.006	0.43 ± 0.01	0.999 ± 0.001	4.4 ± 0.2	15.3 ± 0.3	9.2 ± 1.00	24/18
STAR		\bar{p}	0.127 ± 0.005	0.37 ± 0.01	0.998 ± 0.002	5.1 ± 0.1	16.9 ± 0.2	0.79 ± 0.09	21/16
1(c)	40–100%	π^+	0.103 ± 0.006	0.42 ± 0.01	0.999 ± 0.001	3.7 ± 0.2	13.4 ± 0.3	2.78 ± 0.28	26/18
		p	0.115 ± 0.007	0.37 ± 0.01	0.998 ± 0.002	6.9 ± 0.1	18.2 ± 0.3	0.25 ± 0.03	33/16
1(d)	40–100%	π^-	0.103 ± 0.006	0.42 ± 0.01	0.999 ± 0.001	3.7 ± 0.2	13.4 ± 0.3	2.78 ± 0.28	22/18
		\bar{p}	0.112 ± 0.006	0.35 ± 0.01	0.998 ± 0.002	6.4 ± 0.1	18.9 ± 0.3	0.24 ± 0.02	39/16
2(a)		π^+	0.104 ± 0.006	0.40 ± 0.01	0.999 ± 0.001	2.2 ± 0.1	11.2 ± 0.3	0.64 ± 0.07	22/23
<i>pp</i>	200 GeV	K^+	0.114 ± 0.008	0.41 ± 0.01	0.999 ± 0.001	3.0 ± 0.1	12.4 ± 0.3	0.07 ± 0.01	8/18
STAR		p	0.116 ± 0.008	0.34 ± 0.01	0.999 ± 0.001	3.1 ± 0.2	12.6 ± 0.3	0.05 ± 0.01	29/22
2(b)		π^-	0.104 ± 0.006	0.40 ± 0.01	0.999 ± 0.001	2.2 ± 0.1	11.3 ± 0.3	0.64 ± 0.07	27/23
		K^-	0.114 ± 0.008	0.41 ± 0.01	0.999 ± 0.001	3.2 ± 0.1	13.5 ± 0.3	0.07 ± 0.01	4/18
		\bar{p}	0.116 ± 0.008	0.34 ± 0.01	0.998 ± 0.002	3.1 ± 0.2	13.7 ± 0.4	0.04 ± 0.01	46/22
3(a)	0–5%	π^\pm	0.136 ± 0.008	0.43 ± 0.01	0.999 ± 0.001	2.1 ± 0.1	7.6 ± 0.3	18.70 ± 1.99	320/49*
<i>p</i> -Pb	5.02 TeV	K^\pm	0.193 ± 0.009	0.43 ± 0.01	0.997 ± 0.003	2.7 ± 0.1	7.3 ± 0.3	2.84 ± 0.41	71/45
ALICE		$p+\bar{p}$	0.195 ± 0.009	0.42 ± 0.01	0.999 ± 0.001	3.5 ± 0.2	8.8 ± 0.3	1.10 ± 0.11	172/43
3(b)	80–100%	π^\pm	0.112 ± 0.008	0.43 ± 0.01	0.988 ± 0.006	1.3 ± 0.1	7.4 ± 0.3	1.91 ± 0.20	234/52
		K^\pm	0.139 ± 0.008	0.41 ± 0.01	0.990 ± 0.006	3.3 ± 0.1	8.9 ± 0.3	0.25 ± 0.02	119/45
		$p+\bar{p}$	0.156 ± 0.009	0.37 ± 0.01	0.993 ± 0.006	3.9 ± 0.1	10.1 ± 0.3	0.10 ± 0.01	225/43
4		π^\pm	0.111 ± 0.008	0.43 ± 0.01	0.994 ± 0.005	1.9 ± 0.1	8.1 ± 0.3	3.60 ± 0.35	382/57
<i>pp</i>	2.76 TeV	K^\pm	0.143 ± 0.008	0.42 ± 0.01	0.990 ± 0.005	2.9 ± 0.1	8.6 ± 0.3	0.45 ± 0.05	119/52
ALICE		$p+\bar{p}$	0.152 ± 0.009	0.36 ± 0.01	0.991 ± 0.005	2.6 ± 0.1	9.5 ± 0.3	0.19 ± 0.01	214/43
8(a)	0–20%	π^\pm	0.107 ± 0.006	0.41 ± 0.01	0.999 ± 0.001	4.4 ± 0.3	14.5 ± 0.4	103.61 ± 11.37	28/23
Cu-Cu	200 GeV	K^\pm	0.122 ± 0.011	0.41 ± 0.02	0.997 ± 0.003	6.1 ± 0.3	16.3 ± 0.4	12.52 ± 1.26	1/10
		$p+\bar{p}$	0.125 ± 0.008	0.38 ± 0.01	0.999 ± 0.001	5.2 ± 0.3	15.7 ± 0.4	7.85 ± 0.77	5/21
8(b)	40–94%	π^\pm	0.101 ± 0.005	0.43 ± 0.01	0.999 ± 0.001	4.3 ± 0.2	14.5 ± 0.3	8.29 ± 0.81	18/23
		K^\pm	0.111 ± 0.008	0.40 ± 0.01	0.996 ± 0.003	5.9 ± 0.2	16.9 ± 0.3	1.28 ± 0.11	1/10
		$p+\bar{p}$	0.114 ± 0.009	0.37 ± 0.01	0.996 ± 0.003	6.4 ± 0.2	19.9 ± 0.2	0.50 ± 0.05	15/21

Table 2. Same as Table 1, but showing the values of parameters (T_0 , q , β_T , k , p_0 , and n), normalization constant (N_0), χ^2 , and dof corresponding to the fits of the TBW model and inverse power-law [Eqs. (2) and (5) through Eq. (6) or (7)] in Figs. 1–4 and 8, where the columns of centrality and particle which are the same as Table 1 are omitted to reduce the width of the table.

Figure	T_0 (GeV)	q	β_T (c)	k	p_0 (GeV/c)	n	N_0	χ^2/dof
1(a)	0.108 ± 0.006	1.025 ± 0.007	0.46 ± 0.01	0.991 ± 0.005	4.8 ± 0.3	16.2 ± 0.4	3.86 ± 0.39	46/17
d -Au	0.118 ± 0.008	1.026 ± 0.008	0.46 ± 0.01	0.981 ± 0.006	5.9 ± 0.3	16.0 ± 0.4	0.57 ± 0.06	24/14
PHENIX	0.119 ± 0.008	1.018 ± 0.007	0.45 ± 0.01	0.996 ± 0.004	5.1 ± 0.2	15.9 ± 0.4	0.25 ± 0.02	19/17
1(b)	0.108 ± 0.006	1.025 ± 0.007	0.46 ± 0.01	0.992 ± 0.005	4.8 ± 0.3	16.4 ± 0.4	3.86 ± 0.39	56/17
	0.118 ± 0.008	1.026 ± 0.008	0.46 ± 0.01	0.983 ± 0.009	5.9 ± 0.3	17.0 ± 0.4	0.57 ± 0.06	34/14
	0.118 ± 0.008	1.018 ± 0.007	0.45 ± 0.01	0.996 ± 0.004	5.1 ± 0.2	16.3 ± 0.4	0.20 ± 0.02	36/17
1(c)	0.088 ± 0.006	1.045 ± 0.008	0.46 ± 0.01	0.994 ± 0.004	3.5 ± 0.2	13.7 ± 0.3	1.02 ± 0.10	34/17
	0.090 ± 0.008	1.029 ± 0.008	0.46 ± 0.01	0.955 ± 0.011	6.4 ± 0.3	17.5 ± 0.4	0.13 ± 0.01	9/14
	0.098 ± 0.008	1.012 ± 0.007	0.44 ± 0.01	0.990 ± 0.006	5.5 ± 0.2	15.9 ± 0.2	0.06 ± 0.01	37/17
1(d)	0.088 ± 0.006	1.045 ± 0.008	0.46 ± 0.01	0.994 ± 0.006	3.5 ± 0.2	13.7 ± 0.3	1.02 ± 0.10	46/17
	0.090 ± 0.008	1.029 ± 0.008	0.46 ± 0.01	0.957 ± 0.011	6.7 ± 0.3	18.6 ± 0.4	0.13 ± 0.01	11/14
	0.097 ± 0.008	1.012 ± 0.007	0.43 ± 0.01	0.992 ± 0.006	5.5 ± 0.2	17.1 ± 0.3	0.05 ± 0.01	48/17
1(a)	0.106 ± 0.006	1.020 ± 0.008	0.46 ± 0.01	0.995 ± 0.004	4.4 ± 0.2	15.6 ± 0.4	7.07 ± 0.76	38/17
d -Au	0.115 ± 0.008	1.010 ± 0.007	0.38 ± 0.01	0.998 ± 0.002	4.4 ± 0.2	15.6 ± 0.4	0.96 ± 0.10	35/11*
1(b)	0.106 ± 0.006	1.020 ± 0.008	0.46 ± 0.01	0.995 ± 0.004	4.4 ± 0.2	15.6 ± 0.4	7.07 ± 0.76	39/17
STAR	0.116 ± 0.008	1.008 ± 0.005	0.44 ± 0.01	0.997 ± 0.003	5.1 ± 0.2	17.7 ± 0.4	0.73 ± 0.07	44/15
1(c)	0.085 ± 0.006	1.038 ± 0.008	0.46 ± 0.01	0.996 ± 0.004	3.7 ± 0.2	13.9 ± 0.3	2.50 ± 0.25	33/17
	0.090 ± 0.008	1.008 ± 0.007	0.35 ± 0.01	0.998 ± 0.002	6.9 ± 0.2	19.6 ± 0.4	0.31 ± 0.02	29/11*
1(d)	0.085 ± 0.006	1.038 ± 0.008	0.46 ± 0.01	0.996 ± 0.004	3.7 ± 0.2	13.9 ± 0.3	2.54 ± 0.25	48/17
	0.094 ± 0.008	1.016 ± 0.007	0.44 ± 0.01	0.996 ± 0.004	5.9 ± 0.2	19.4 ± 0.3	0.19 ± 0.02	53/15
2(a)	0.089 ± 0.006	1.023 ± 0.008	0.44 ± 0.01	0.997 ± 0.003	2.2 ± 0.1	11.2 ± 0.4	0.62 ± 0.06	41/22
pp	0.098 ± 0.008	1.029 ± 0.009	0.43 ± 0.01	0.996 ± 0.004	3.0 ± 0.2	12.8 ± 0.4	0.07 ± 0.01	29/17
STAR	0.104 ± 0.009	1.006 ± 0.001	0.39 ± 0.01	0.996 ± 0.004	3.1 ± 0.2	13.5 ± 0.4	0.05 ± 0.01	55/21
2(b)	0.089 ± 0.006	1.023 ± 0.008	0.44 ± 0.01	0.997 ± 0.003	2.2 ± 0.1	11.5 ± 0.4	0.62 ± 0.06	52/22
	0.098 ± 0.008	1.029 ± 0.009	0.43 ± 0.01	0.996 ± 0.004	3.0 ± 0.2	13.8 ± 0.4	0.07 ± 0.01	26/17
	0.104 ± 0.009	1.006 ± 0.001	0.39 ± 0.01	0.996 ± 0.004	3.1 ± 0.2	13.9 ± 0.4	0.04 ± 0.01	84/21
3(a)	0.107 ± 0.007	1.001 ± 0.001	0.48 ± 0.01	0.999 ± 0.001	2.2 ± 0.1	7.7 ± 0.3	20.98 ± 2.00	323/47*
p -Pb	0.188 ± 0.009	1.012 ± 0.006	0.48 ± 0.01	0.995 ± 0.004	2.7 ± 0.2	7.8 ± 0.3	2.78 ± 0.29	436/44
ALICE	0.198 ± 0.009	1.013 ± 0.008	0.47 ± 0.01	0.999 ± 0.001	3.5 ± 0.2	9.1 ± 0.3	1.10 ± 0.10	223/42
3(b)	0.089 ± 0.006	1.001 ± 0.001	0.45 ± 0.01	0.999 ± 0.001	1.4 ± 0.1	7.3 ± 0.3	2.21 ± 0.20	606/43*
	0.113 ± 0.008	1.023 ± 0.006	0.45 ± 0.01	0.976 ± 0.010	3.3 ± 0.2	9.1 ± 0.3	0.23 ± 0.02	325/44
	0.115 ± 0.009	1.002 ± 0.001	0.45 ± 0.01	0.982 ± 0.010	3.9 ± 0.2	10.6 ± 0.3	0.09 ± 0.01	493/42
4	0.089 ± 0.006	1.001 ± 0.001	0.45 ± 0.01	0.999 ± 0.001	1.7 ± 0.1	7.8 ± 0.3	4.00 ± 0.31	485/48*
pp	0.113 ± 0.008	1.013 ± 0.006	0.48 ± 0.01	0.975 ± 0.010	2.9 ± 0.1	9.0 ± 0.3	0.46 ± 0.05	376/51
ALICE	0.116 ± 0.008	1.004 ± 0.001	0.44 ± 0.01	0.975 ± 0.010	2.5 ± 0.2	9.9 ± 0.3	0.20 ± 0.02	494/42
8(a)	0.101 ± 0.007	1.027 ± 0.009	0.47 ± 0.02	0.999 ± 0.001	4.4 ± 0.2	14.8 ± 0.4	66.17 ± 7.10	27/22
Cu-Cu	0.110 ± 0.008	1.026 ± 0.008	0.46 ± 0.02	0.996 ± 0.004	6.2 ± 0.3	16.5 ± 0.4	12.23 ± 1.20	3/9
	0.114 ± 0.008	1.020 ± 0.007	0.45 ± 0.01	0.999 ± 0.001	5.2 ± 0.3	16.3 ± 0.4	6.02 ± 0.60	4/20
8(b)	0.085 ± 0.007	1.052 ± 0.008	0.47 ± 0.02	0.999 ± 0.001	4.3 ± 0.2	14.7 ± 0.3	6.58 ± 0.68	19/22
	0.090 ± 0.008	1.029 ± 0.008	0.47 ± 0.02	0.996 ± 0.004	6.0 ± 0.3	16.7 ± 0.3	1.08 ± 0.01	3/9
	0.095 ± 0.008	1.012 ± 0.008	0.46 ± 0.01	0.992 ± 0.004	6.6 ± 0.2	21.3 ± 0.4	0.38 ± 0.04	12/20

Table 3. Same as Table 1, but showing the values of parameters (T , k , p_0 , and n), normalization constant (N_0), χ^2 , and dof corresponding to the fits of the Boltzmann distribution and inverse power-law [Eqs. (3) and (5) through Eq. (6) or (7)] in Figs. 1–4 and 8.

Figure	Centrality	Particle	T (GeV)	k	p_0 (GeV/c)	n	N_0	χ^2/dof
1(a)	0–20%	π^+	0.179 ± 0.006	0.992 ± 0.005	4.9 ± 0.2	16.8 ± 0.3	3.70 ± 0.35	28/17*
<i>d</i> -Au	200 GeV	K^+	0.243 ± 0.009	0.976 ± 0.011	5.9 ± 0.2	16.9 ± 0.3	0.60 ± 0.05	39/16
PHENIX		p	0.293 ± 0.009	0.991 ± 0.006	5.1 ± 0.2	15.8 ± 0.3	0.25 ± 0.02	24/19
1(b)	0–20%	π^-	0.179 ± 0.006	0.993 ± 0.006	4.8 ± 0.2	16.8 ± 0.3	3.70 ± 0.35	29/17*
		K^-	0.240 ± 0.009	0.974 ± 0.011	5.6 ± 0.2	16.9 ± 0.3	0.58 ± 0.05	37/16
		\bar{p}	0.290 ± 0.009	0.993 ± 0.005	5.0 ± 0.2	16.5 ± 0.3	0.20 ± 0.02	30/19
1(c)	60–88%	π^+	0.148 ± 0.006	0.995 ± 0.005	3.5 ± 0.1	13.5 ± 0.2	1.14 ± 0.01	61/17*
		K^+	0.200 ± 0.009	0.950 ± 0.011	6.4 ± 0.3	17.7 ± 0.3	0.15 ± 0.01	18/16
		p	0.247 ± 0.009	0.993 ± 0.005	5.3 ± 0.2	15.5 ± 0.3	0.07 ± 0.01	42/19
1(d)	60–88%	π^-	0.148 ± 0.006	0.995 ± 0.004	3.5 ± 0.1	13.5 ± 0.2	1.14 ± 0.01	70/17*
		K^-	0.200 ± 0.009	0.954 ± 0.012	6.2 ± 0.3	17.9 ± 0.3	0.14 ± 0.01	17/16
		\bar{p}	0.247 ± 0.009	0.993 ± 0.005	5.0 ± 0.2	16.5 ± 0.3	0.05 ± 0.01	28/19
1(a)	0–20%	π^+	0.172 ± 0.007	0.999 ± 0.001	4.1 ± 0.1	15.0 ± 0.3	7.70 ± 0.70	42/17*
<i>d</i> -Au	200 GeV	p	0.208 ± 0.009	0.999 ± 0.001	5.8 ± 0.2	16.5 ± 0.3	1.07 ± 0.10	28/15*
1(b)	0–20%	π^-	0.172 ± 0.007	0.999 ± 0.001	4.1 ± 0.1	15.0 ± 0.3	7.70 ± 0.70	36/17*
STAR		\bar{p}	0.253 ± 0.008	0.997 ± 0.003	5.2 ± 0.2	17.2 ± 0.3	0.73 ± 0.06	33/17
1(c)	40–100%	π^+	0.143 ± 0.007	0.998 ± 0.002	3.1 ± 0.1	12.4 ± 0.2	2.63 ± 0.24	59/17*
		p	0.219 ± 0.009	0.991 ± 0.005	5.8 ± 0.2	17.8 ± 0.3	0.27 ± 0.02	37/17
1(d)	40–100%	π^-	0.143 ± 0.007	0.998 ± 0.002	3.1 ± 0.1	12.4 ± 0.2	2.63 ± 0.24	49/17*
		\bar{p}	0.217 ± 0.009	0.992 ± 0.005	5.4 ± 0.1	18.5 ± 0.3	0.22 ± 0.02	30/17
2(a)		π^+	0.144 ± 0.007	0.999 ± 0.001	2.0 ± 0.1	10.8 ± 0.3	0.55 ± 0.33	35/22*
<i>pp</i>	200 GeV	K^+	0.203 ± 0.009	0.989 ± 0.007	3.3 ± 0.1	13.3 ± 0.3	0.07 ± 0.01	31/19
STAR		p	0.234 ± 0.009	0.997 ± 0.003	3.2 ± 0.2	13.6 ± 0.3	0.05 ± 0.01	121/23
2(b)		π^-	0.144 ± 0.007	0.999 ± 0.001	2.0 ± 0.1	10.8 ± 0.3	0.55 ± 0.33	47/22*
		K^-	0.203 ± 0.009	0.991 ± 0.005	3.1 ± 0.1	13.7 ± 0.3	0.07 ± 0.01	21/19
		\bar{p}	0.230 ± 0.009	0.996 ± 0.004	3.1 ± 0.2	14.3 ± 0.3	0.04 ± 0.01	91/23
3(a)	0–5%	π^\pm	0.163 ± 0.008	0.999 ± 0.001	2.0 ± 0.1	7.7 ± 0.3	22.14 ± 2.10	852/49*
<i>p</i> -Pb	5.02 TeV	K^\pm	0.297 ± 0.008	0.992 ± 0.005	3.4 ± 0.1	8.6 ± 0.3	2.87 ± 0.29	110/44*
ALICE		$p+\bar{p}$	0.381 ± 0.009	0.997 ± 0.003	3.2 ± 0.1	9.4 ± 0.3	1.17 ± 0.01	138/42*
3(b)	80–100%	π^\pm	0.123 ± 0.009	0.999 ± 0.001	1.4 ± 0.1	7.2 ± 0.3	2.23 ± 0.19	935/49*
		K^\pm	0.212 ± 0.010	0.995 ± 0.005	3.8 ± 0.1	9.0 ± 0.3	0.28 ± 0.02	403/44*
		$p+\bar{p}$	0.235 ± 0.010	0.997 ± 0.003	3.3 ± 0.1	9.8 ± 0.3	0.11 ± 0.01	128/42*
4		π^\pm	0.123 ± 0.008	0.997 ± 0.003	1.7 ± 0.1	7.9 ± 0.3	4.14 ± 0.31	688/54*
<i>pp</i>	2.76 TeV	K^\pm	0.205 ± 0.009	0.988 ± 0.010	2.8 ± 0.1	8.7 ± 0.3	0.49 ± 0.06	178/51*
ALICE		$p+\bar{p}$	0.241 ± 0.009	0.995 ± 0.005	2.6 ± 0.1	9.5 ± 0.3	0.20 ± 0.02	104/42*
8(a)	0–20%	π^\pm	0.179 ± 0.008	0.999 ± 0.001	4.2 ± 0.1	14.5 ± 0.2	72.07 ± 7.00	35/22*
Cu-Cu	200 GeV	K^\pm	0.231 ± 0.010	0.991 ± 0.006	5.9 ± 0.2	16.9 ± 0.3	12.37 ± 1.21	5/11
		$p+\bar{p}$	0.296 ± 0.009	0.999 ± 0.001	5.4 ± 0.2	17.0 ± 0.4	5.81 ± 0.67	6/22
8(b)	40–94%	π^\pm	0.139 ± 0.006	0.999 ± 0.001	3.8 ± 0.1	13.9 ± 0.2	10.95 ± 0.89	23/22*
		K^\pm	0.179 ± 0.009	0.994 ± 0.005	4.9 ± 0.1	16.2 ± 0.3	1.16 ± 0.13	1/9*
		$p+\bar{p}$	0.245 ± 0.008	0.999 ± 0.001	4.8 ± 0.2	17.7 ± 0.3	0.43 ± 0.06	3/20*

Table 4. Same as Table 1, but showing the values of parameters (T , q , k , p_0 , and n), normalization constant (N_0), χ^2 , and dof corresponding to the fits of the Tsallis distribution and inverse power-law [Eqs. (4) and (5) through Eq. (6) or (7)] in Figs. 1–4 and 8.

Figure	Centrality	Particle	T (GeV)	q	k	p_0 (GeV/ c)	n	N_0	χ^2/dof
1(a)	0–20%	π^+	0.134 ± 0.008	1.082 ± 0.009	0.994 ± 0.005	4.8 ± 0.2	16.3 ± 0.4	3.93 ± 0.36	32/18
<i>d</i> -Au	200 GeV	K^+	0.189 ± 0.009	1.052 ± 0.010	0.980 ± 0.010	6.1 ± 0.2	16.9 ± 0.4	0.57 ± 0.06	13/15
PHENIX		p	0.272 ± 0.009	1.015 ± 0.007	0.999 ± 0.001	5.5 ± 0.2	15.3 ± 0.4	0.28 ± 0.02	49/18
1(b)	0–20%	π^-	0.134 ± 0.008	1.082 ± 0.009	0.993 ± 0.005	4.8 ± 0.2	16.8 ± 0.4	3.68 ± 0.36	33/18
		K^-	0.189 ± 0.009	1.052 ± 0.010	0.982 ± 0.011	6.0 ± 0.2	17.1 ± 0.4	0.56 ± 0.06	18/15
		\bar{p}	0.273 ± 0.009	1.015 ± 0.007	0.999 ± 0.001	5.4 ± 0.2	16.0 ± 0.4	0.18 ± 0.02	44/18
1(c)	60–88%	π^+	0.108 ± 0.008	1.099 ± 0.009	0.999 ± 0.001	3.6 ± 0.1	13.1 ± 0.3	1.20 ± 0.12	37/18
		K^+	0.141 ± 0.009	1.083 ± 0.011	0.984 ± 0.012	6.6 ± 0.2	17.5 ± 0.4	0.15 ± 0.02	16/15
		p	0.194 ± 0.010	1.035 ± 0.010	0.996 ± 0.004	5.8 ± 0.2	15.9 ± 0.4	0.07 ± 0.01	22/18
1(d)	60–88%	π^-	0.108 ± 0.008	1.099 ± 0.009	0.999 ± 0.001	3.5 ± 0.1	12.9 ± 0.3	1.17 ± 0.12	36/18
		K^-	0.141 ± 0.009	1.083 ± 0.011	0.979 ± 0.012	6.5 ± 0.2	17.8 ± 0.4	0.13 ± 0.02	11/15
		\bar{p}	0.194 ± 0.010	1.035 ± 0.010	0.998 ± 0.002	5.8 ± 0.2	16.6 ± 0.4	0.05 ± 0.01	30/18
1(a)	0–20%	π^+	0.129 ± 0.008	1.076 ± 0.009	0.997 ± 0.003	4.4 ± 0.1	15.4 ± 0.4	8.03 ± 0.80	26/18
<i>d</i> -Au	200 GeV	p	0.221 ± 0.009	1.005 ± 0.005	0.999 ± 0.001	5.9 ± 0.2	16.8 ± 0.3	1.01 ± 0.09	23/13*
1(b)	0–20%	π^-	0.129 ± 0.008	1.076 ± 0.009	0.997 ± 0.003	4.4 ± 0.1	15.4 ± 0.4	8.03 ± 0.80	27/18
STAR		\bar{p}	0.260 ± 0.009	1.009 ± 0.005	0.999 ± 0.001	5.7 ± 0.2	17.3 ± 0.3	0.68 ± 0.07	46/16
1(c)	40–100%	π^+	0.104 ± 0.008	1.089 ± 0.009	0.998 ± 0.002	3.4 ± 0.1	13.1 ± 0.3	2.62 ± 0.25	32/18
		p	0.173 ± 0.009	1.011 ± 0.005	0.999 ± 0.001	6.3 ± 0.2	17.0 ± 0.3	0.31 ± 0.03	33/13*
1(d)	40–100%	π^-	0.104 ± 0.008	1.089 ± 0.009	0.998 ± 0.002	3.4 ± 0.1	13.1 ± 0.3	2.62 ± 0.25	26/18
		\bar{p}	0.189 ± 0.009	1.036 ± 0.005	0.999 ± 0.001	5.4 ± 0.2	17.7 ± 0.3	0.19 ± 0.02	35/16
2(a)		π^+	0.120 ± 0.008	1.051 ± 0.009	0.997 ± 0.003	2.1 ± 0.1	10.9 ± 0.3	0.60 ± 0.05	44/23
<i>pp</i>	200 GeV	K^+	0.153 ± 0.009	1.057 ± 0.011	0.997 ± 0.003	3.5 ± 0.1	13.2 ± 0.3	0.07 ± 0.01	14/18
STAR		p	0.190 ± 0.009	1.019 ± 0.009	0.997 ± 0.003	3.3 ± 0.1	13.3 ± 0.4	0.05 ± 0.01	32/22
2(b)		π^-	0.120 ± 0.008	1.056 ± 0.009	0.997 ± 0.003	2.1 ± 0.1	11.0 ± 0.3	0.56 ± 0.05	45/23
		K^-	0.153 ± 0.009	1.057 ± 0.011	0.998 ± 0.002	3.5 ± 0.1	13.9 ± 0.3	0.07 ± 0.01	7/18
		\bar{p}	0.190 ± 0.009	1.019 ± 0.009	0.997 ± 0.003	3.3 ± 0.1	13.9 ± 0.4	0.04 ± 0.01	42/22
3(a)	0–5%	π^\pm	0.156 ± 0.008	1.031 ± 0.012	0.999 ± 0.001	2.2 ± 0.1	7.7 ± 0.3	21.20 ± 1.91	934/45*
<i>p</i> -Pb	5.02 TeV	K^\pm	0.262 ± 0.008	1.059 ± 0.011	0.995 ± 0.005	3.0 ± 0.1	7.8 ± 0.3	2.78 ± 0.28	261/45
ALICE		$p+\bar{p}$	0.351 ± 0.009	1.035 ± 0.009	0.999 ± 0.001	3.4 ± 0.1	9.1 ± 0.3	1.09 ± 0.01	97/43
3(b)	80–100%	π^\pm	0.111 ± 0.008	1.042 ± 0.009	0.998 ± 0.002	1.4 ± 0.1	7.3 ± 0.3	2.15 ± 0.20	389/49*
		K^\pm	0.171 ± 0.008	1.068 ± 0.012	0.986 ± 0.010	3.8 ± 0.1	9.3 ± 0.3	0.23 ± 0.02	282/45
		$p+\bar{p}$	0.192 ± 0.009	1.056 ± 0.011	0.993 ± 0.005	3.4 ± 0.1	9.8 ± 0.3	0.10 ± 0.01	230/43
4		π^\pm	0.112 ± 0.008	1.042 ± 0.004	0.997 ± 0.003	1.7 ± 0.1	7.9 ± 0.3	3.90 ± 0.36	461/54*
<i>pp</i>	2.76 TeV	K^\pm	0.175 ± 0.009	1.071 ± 0.011	0.985 ± 0.010	2.8 ± 0.1	8.7 ± 0.3	0.44 ± 0.06	253/52
ALICE		$p+\bar{p}$	0.223 ± 0.009	1.029 ± 0.008	0.988 ± 0.010	2.6 ± 0.1	9.5 ± 0.3	0.19 ± 0.02	373/43
8(a)	0–20%	π^+	0.131 ± 0.007	1.070 ± 0.006	0.999 ± 0.001	4.4 ± 0.2	14.6 ± 0.3	73.32 ± 8.01	23/23
Cu-Cu	200 GeV	K^+	0.173 ± 0.011	1.055 ± 0.010	0.997 ± 0.003	6.4 ± 0.2	16.9 ± 0.4	12.42 ± 1.31	1/10
		p	0.250 ± 0.009	1.018 ± 0.006	0.995 ± 0.005	5.4 ± 0.2	16.4 ± 0.3	6.30 ± 0.75	6/21
8(b)	40–94%	π^+	0.105 ± 0.006	1.096 ± 0.006	0.999 ± 0.001	4.4 ± 0.3	14.1 ± 0.4	7.90 ± 0.83	23/23
		K^+	0.139 ± 0.009	1.076 ± 0.009	0.998 ± 0.002	5.2 ± 0.3	15.9 ± 0.4	1.08 ± 0.12	1/10
		p	0.197 ± 0.009	1.042 ± 0.006	0.995 ± 0.005	5.1 ± 0.2	17.9 ± 0.3	0.43 ± 0.04	9/21

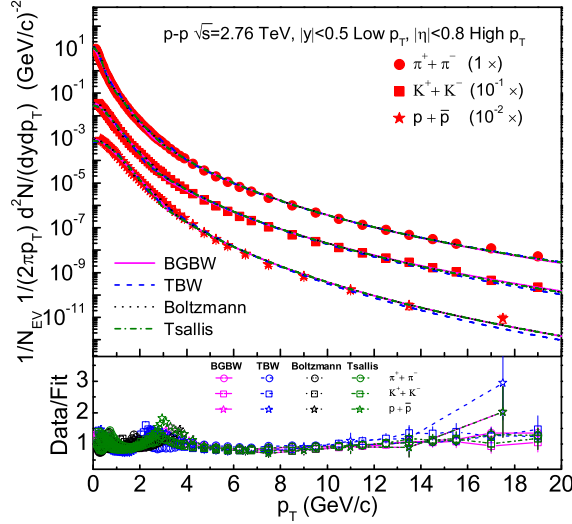


Fig. 4. (Color online) Same as Fig. 1, but showing the spectra of $\pi^+ + \pi^-$, $K^+ + K^-$, and $p + \bar{p}$ produced in pp collisions at $\sqrt{s} = 2.76$ TeV. The symbols represent the experimental data of the ALICE Collaboration measured in $|y| < 0.5$ for low- p_T particles and in $|\eta| < 0.8$ for high- p_T particles [25].

free parameters in each fit, these parameters are restricted and irrelevant. In fact, some of them (1–3 parameters) are sensitive to the very-soft component which describes the very-low p_T range from 0 to 0.5–1.5 GeV/c in some cases. Some of them (1–3 parameters) are sensitive to the soft component which describes the low p_T range from 0.5–1.5 GeV/c to 2.5–3.5 GeV/c in some cases or from 0 to 2.5–3.5 GeV/c in most cases. While the final two parameters (p_0 and n) are sensitive to the hard component which describes the wide p_T range from 2.5–3.5 GeV/c to the maximum. In some cases, the data in the very-low p_T range is not available. Then, the number of free parameters will be reduced by 1–3, and we can use the low p_T range from 0 to 2.5–3.5 GeV/c.

The last two models use the relations between T and m_0 , $\langle p_T \rangle$ and \bar{m} , as well as $\langle p \rangle$ and \bar{m} . They are not suitable to fit simultaneously all particles in low p_T range due to the mass dependences of the relations. In principle, we can try doing simultaneous fits of all particles by using the first two models. In the case of doing simultaneous fits, larger χ^2 will be obtained due to the same set of parameters. Although we fit different particle spectra by different sets of parameters, the mean value of a given parameter can be obtained by weighting different yields of considered particles. The weighted mean parameter is thus regarded as the parameter which is suitable for the simultaneous fit of all the particles. So, both the simultaneous and non-simultaneous fits can be used in the analysis of particle spectra.

Based on the descriptions of p_T spectra, the first two

models can give T_0 and β_T conveniently, though the values of parameters are possibly not the same due to different models. To obtain the values of T_0 , β_T , and β by the models iii) and iv), we analyze the values of T presented in Tables 3 and 4, and calculate $\langle p_T \rangle$, $\langle p \rangle$, and \bar{m} based on the values of parameters listed in Tables 3 and 4. That is, we derive $\langle p_T \rangle$, $\langle p \rangle$, and \bar{m} by more complex fitting of Boltzmann and Tsallis distributions in the p_T range from 0 to p_1 , but not the simple counting of published spectra due to the data being possibly unavailable in some regions. In fact, based on an isotropic assumption in the rest frame of emission source and using the Monte Carlo method, we can perform the calculations from p_T to $\langle p \rangle$ and \bar{m} [15–17]. One can see that there are other constraints in the statistical fits due to the excluding contribution of hard component and the selecting reference frame of emission source.

The relations between T and m_0 , $\langle p_T \rangle$ and \bar{m} , as well as $\langle p \rangle$ and \bar{m} are shown in Figs. 5, 6, and 7, respectively, where panels (a) and (b) correspond to the models iii) and iv) which use the Boltzmann and Tsallis distributions, respectively. The symbols in Fig. 5 represent values of T listed in Tables 3 and 4 for different m_0 . The symbols in Figs. 6 and 7 represent values of $\langle p_T \rangle$ and $\langle p \rangle$ for different \bar{m} , respectively, which are calculated due to the parameters listed in Tables 3 and 4 and the isotropic assumption in the rest frame of emission source. The error bars in the three figures are overall errors. The lines in the three figures connect the points for visibility in each event sample, though the method

of least squares is used to give a good connection. The intercept in Fig. 5 reflects T_0 , and the slopes in Figs. 6 and 7 reflect β_T and β , respectively. The values of T , T_0 , β_T , β , and \overline{m} are approximately independent of isospin.

To compare values of key parameters obtained by different models for different event samples, we now discuss the qualitative dependences of T_0 and β_T on the centrality. From Tables 1 and 2, we can obtain T_0 and β_T in the first two models by weighting yields of different particles. From Fig. 5 T_0 can be obtained in the last two models by the intercept. While, from Fig. 6 (or 7) we can obtain β_T (or β) in the last two models by the slope. Generally, the four models present similar results, and in some cases these results are in agreement with each other within errors. In central d -Au and p -Pb collisions, T_0 is relatively larger than that in peripheral collisions. From the RHIC to LHC energies, T_0 shows a slightly increase or nearly invariant. From peripheral to central collisions and from the RHIC to LHC energies, both β_T show a slightly increase or nearly invariant. These situations are in agreement with our recent work which studied Au-Au collisions at the RHIC and Pb-Pb collisions at the LHC [14] by a somehow different superposition. In particular, the absolute values of T_0 and β_T do not show obvious change from d -Au (p -Pb) to Au-Au (Pb-Pb) collisions, except for the systematical increase ($\leq 5\%$) due to different superpositions. In pp collisions, the dependences of T_0 and β_T on \sqrt{s} are similar to those in peripheral nuclear (d -Au, Au-Au, p -Pb, and Pb-Pb) collisions.

In the above discussions, it looks that T_0 and β_T are related to physical properties of an expanding thermal system which is a high energy collision system with given impact parameter in the present work. In the case of considering a mini-bias data sample, T_0 and β_T are average over various impact parameters. In particular, T_0 and β_T in central (peripheral) collisions are average over a given centrality range. For pp collisions without centrality selection, T_0 and β_T are average over given data sample and they are related to physical properties of the sample. In terms of excitation degree which is characterized by T_0 , nuclear collisions such as d -Au and Au-Au collisions at the RHIC and p -Pb and Pb-Pb collisions at the LHC show similar excitation degree at the kinetic freeze-out, though the excitation degree in central collisions is slightly higher than that in peripheral collisions. The excitation degree is dependent of the heaviest nucleus, but not the total nucleus, minimum nucleus, numbers of participant nucleons, and binary collisions, in nuclear collisions at a given energy.

To confirm the above statement of the heaviest nucleus instead of total nucleus to determine T_0 , we now analyze copper-copper (Cu-Cu) collisions. Figure 8 is the same as Fig. 1, but it shows the spectra of $\pi^+ + \pi^-$, $K^+ + K^-$, and $p + \bar{p}$ produced in (a) 0–20% and (b) 40–94% (60–92%, 60–94%, and 40–60%) Cu-Cu collisions at $\sqrt{s_{NN}} = 200$ GeV. The closed and open symbols represent the experimental data of the PHENIX and STAR Collaboration measured in $|\eta| < 0.35$ and $|y| < 0.5$, respectively [29, 30], where the data in 0–20% are obtained by combining different centralities (0–5%, 5–10%, and 10–20%) to play up to Fig. 1, and the data measured by different collaborations are connected by scaling different amounts marked in the panel. The fit parameters are given in Tables 1–4, where the values of N_0 are obtained due to the scaled spectra, but not the original spectra. One can see that the four considered models describe approximately the p_T spectra of identified particles produced in central (0–20%) and peripheral (40–94%) Cu-Cu collisions at $\sqrt{s_{NN}} = 200$ GeV.

Figures 9(a) and 9(b) are the same as Figs. 5 and 6 (or 7), respectively, but they show the relations between T and m_0 , as well as $\langle p_T \rangle$ and \overline{m} ($\langle p \rangle$ and \overline{m}), according to the parameter values of Cu-Cu collisions at $\sqrt{s_{NN}} = 200$ GeV. It can be seen that the mentioned relations show approximately linear tendencies in most cases. In particular, the intercept in Fig. 9(a) reflects T_0 , and the slopes in Fig. 9(b) reflect β_T and β , respectively.

For the qualitative comparison of the results obtained in different types of collisions, Tables 1 and 2, as well as Figs. 5, 6 and 9 are examined on the values of T_0 and β_T . One can see that T_0 in central Cu-Cu collisions are slightly smaller than those in central d -Au (p -Pb) collisions due to the size of Cu is smaller than that of Au (Pb). This is a direct and strong evidence for the statement of the heaviest nucleus instead of total nucleus to determine T_0 . In addition, T_0 in peripheral Cu-Cu collisions are approximately equal to those in peripheral d -Au (p -Pb) collisions and in pp collisions. The dependence of β_T on the size of heaviest nucleus seems to be indeterminate, though β_T in central collisions is comparable with that in peripheral collisions.

The closeness of the results obtained in small system and nucleus-nucleus collisions reveal some universality in hadroproduction process, as it is argued in refs. [31–35]. The universality in hadroproduction process appears in different quantities observed [36] in different types of collisions (including proton-proton, proton-

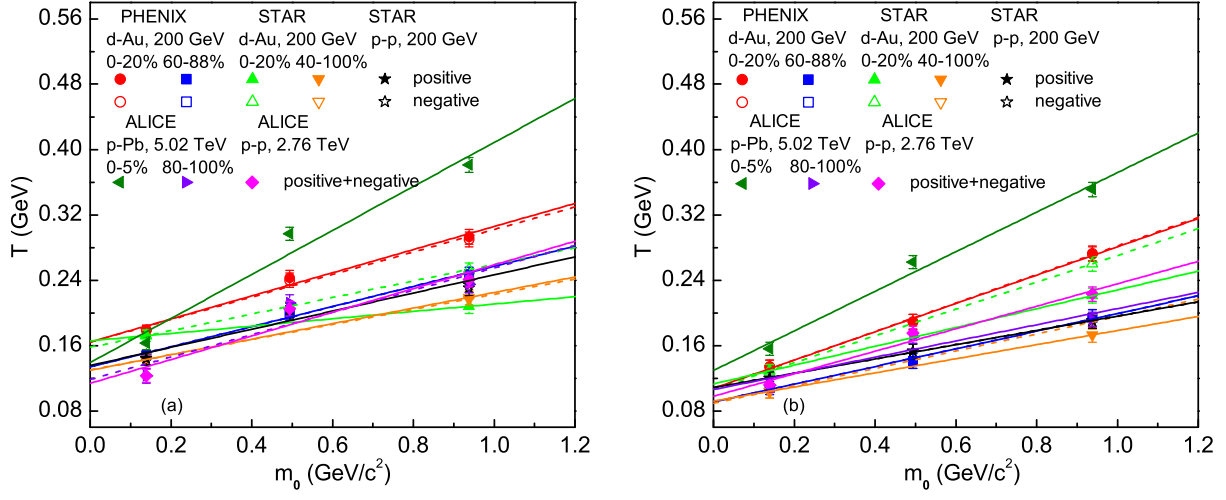


Fig. 5. (Color online) Relations between T and m_0 , where panels (a) and (b) correspond to the models iii) and iv) which use the Boltzmann and Tsallis distributions, respectively. The symbols represent values of T listed in Tables 3 and 4 for different m_0 . The lines connect the points for visibility.

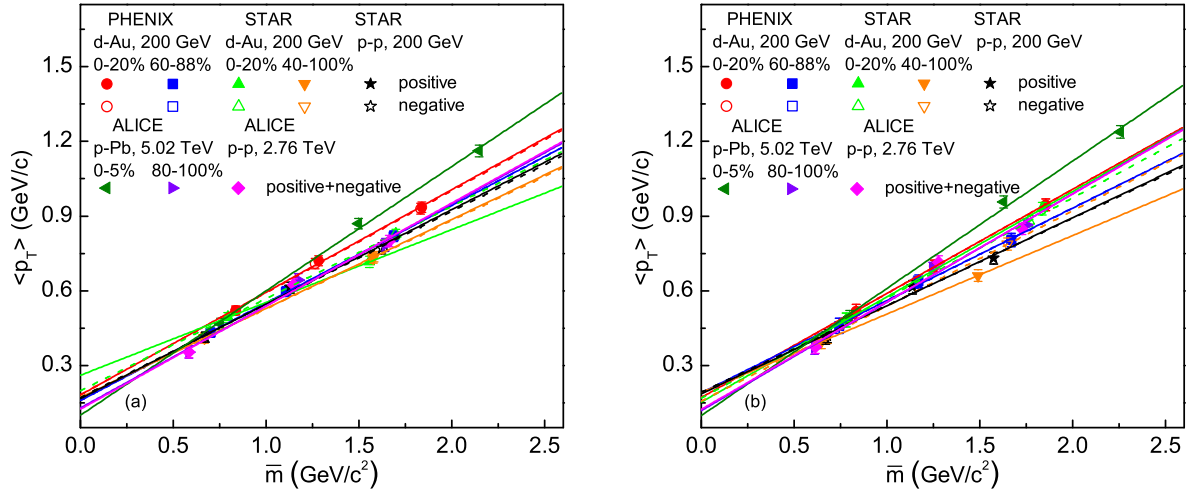


Fig. 6. (Color online) Same as Fig. 5, but showing the relations between $\langle p_T \rangle$ and \bar{m} . The symbols represent values of $\langle p_T \rangle$ for different \bar{m} , which are calculated due to the parameters listed in Tables 3 and 4 and the isotropic assumption in the rest frame of emission source.

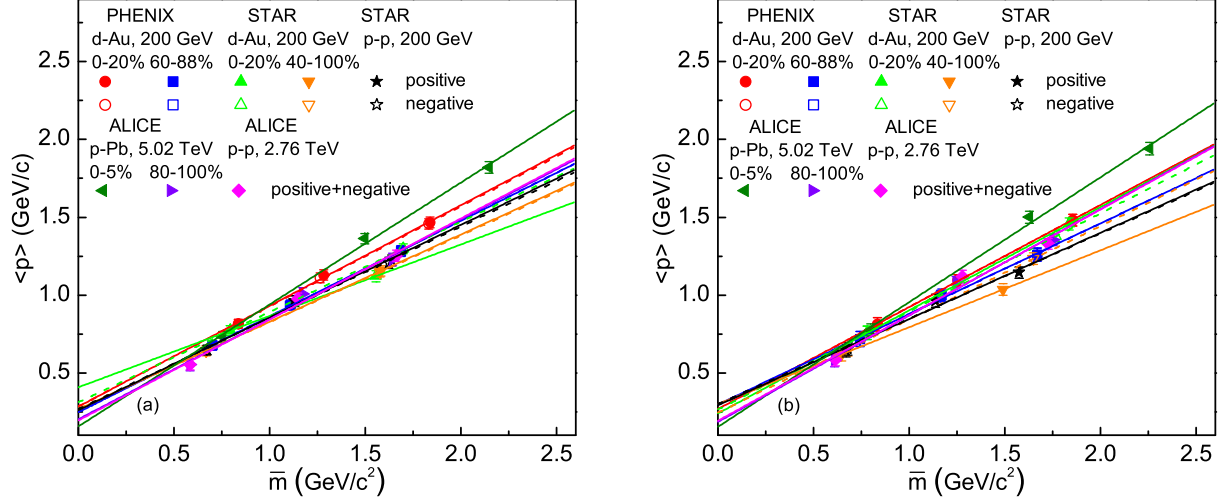


Fig. 7. (Color online) Same as Fig. 5, but showing the relations between $\langle p \rangle$ and \overline{m} . The symbols represent values of $\langle p \rangle$ for different \overline{m} , which are calculated due to the parameters listed in Tables 3 and 4 and the isotropic assumption in the rest frame of emission source.

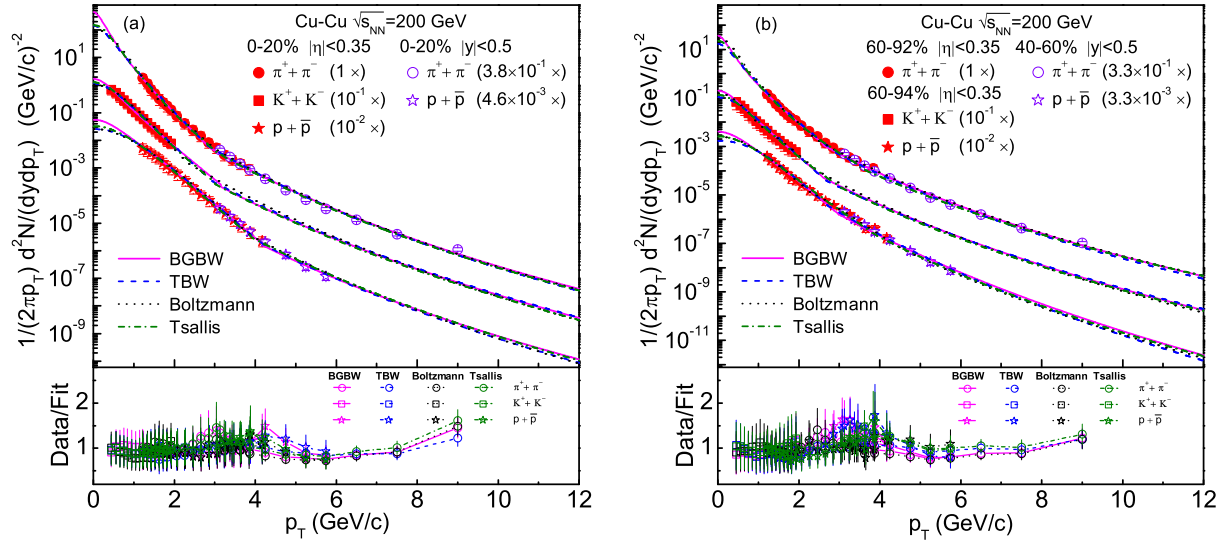


Fig. 8. (Color online) Same as Fig. 1, but showing the spectra of $\pi^+ + \pi^-$, $K^+ + K^-$, and $p + \bar{p}$ produced in (a) 0-20% and (b) 40-94% Cu-Cu collisions at $\sqrt{s_{NN}} = 200$ GeV. The closed and open symbols represent the experimental data of the PHENIX and STAR Collaboration measured in $|\eta| < 0.35$ and $|y| < 0.5$, respectively [29, 30], where the data in 0-20% are obtained by combining different centralities (0-5%, 5-10%, and 10-20%) to play up to Fig. 1, and the data measured by different collaborations are connected by scaling different amounts.

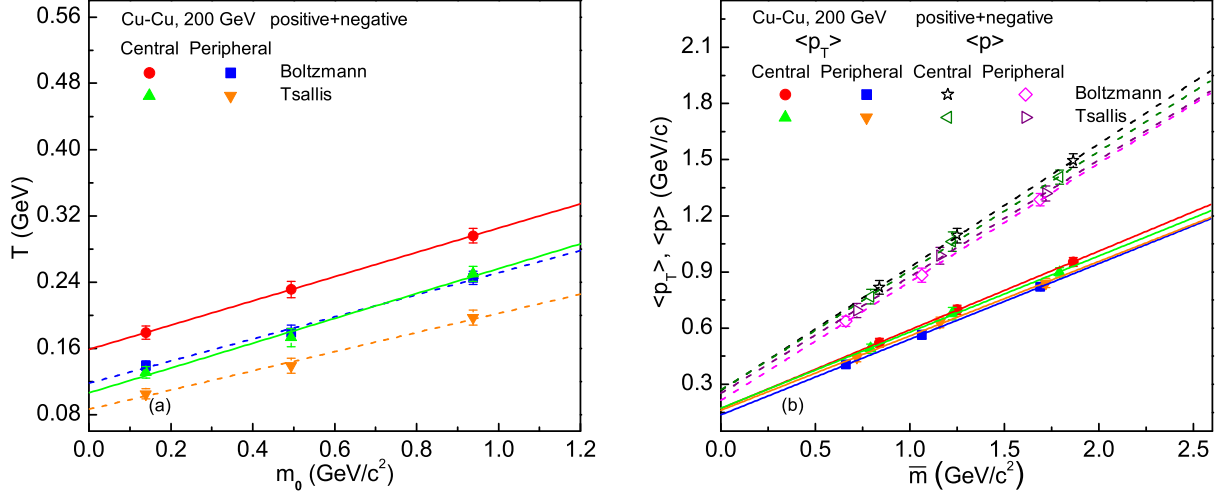


Fig. 9. (Color online) Same as Figs. 5 and 6 (7), but showing the relations between (a) T and m_0 , as well as (b) $\langle p_T \rangle$ and \bar{m} ($\langle p \rangle$ and \bar{m}), according to the parameter values of Cu-Cu collisions at $\sqrt{s_{NN}} = 200$ GeV.

nucleus, and nucleus-nucleus collisions) and/or at different energies (available from the RHIC even RHIC BES and SPS BES to LHC) [31–35]. These quantities include, but are not limited to, mean multiplicity, rapidity or pseudorapidity density, multiplicity or transverse momentum distribution, and event patterns in different spaces in some conditions. The present work confirms that the universality in hadroproduction process exists possibly in thermal parameters at the kinetic freeze-out in different types of collisions from the RHIC to LHC [14].

Although the blast-wave model and related distributions themselves lack contributions from resonance decays and strong stopping effects, we can use a two-component form to describe the spectra in very-low and low p_T ranges. In addition, in d -Au and p -Pb collisions, the cold nuclear modification effects on p_T spectra are not considered by us, though some of them modify p_T spectra of the identified particles to be wider due to multiple cascade collisions in the cold spectator region. If the contribution of cold nuclear modification effects on p_T spectra is excluded, we should obtain smaller T_0 and β_T . From the comparison with pp collisions, one knows that the contribution of cold nuclear modification effects on T_0 and β_T is not obvious due to similar values in peripheral nuclear collisions and pp collisions. Moving a step further, the contribution of cold nuclear modification effects on T_0 and β_T in Au-Au (Pb-Pb) collisions at the RHIC (LHC) is also not obvious [14].

The Tsallis function has connection to thermal model due to its fits to two- or three-component Boltzmann distribution [37]. The index q represents the degree of

non-equilibrium between two or among three states described by Boltzmann distributions, and the Tsallis temperature describes the fluctuations of Boltzmann temperatures. These explanations on the level of drawing curves reveal that the interacting systems at the RHIC and LHC stays in a transitional region from extensive system to non-extensive system. There is no obvious boundary to distinguish extensive system and non-extensive system for a given interacting system in the considered energy range. On the other hand, at the RHIC and its beam energy scan energies or similar energies, the generic axiomatic-nonextensive statistics is used to obtain the chemical freeze-out temperature and baryon chemical potential [38–40]. This renders that the Boltzmann-Gibbs and Tsallis statistics are not always necessary or applicable. We would like to say that the interacting systems at the considered energies are complex. More studies are needed in the future.

In central collisions at RHIC and LHC energies, the four models extract the kinetic freeze-out temperatures around $T_0 \approx 120$ MeV. It is lower than the chemical freeze-out temperature $T_{ch} \approx 160$ MeV [1–4]. This confirms that the kinetic freeze-out happens latter than the chemical freeze-out at the considered energies. As an approximate treatment, we consider an ideal fluid in which the time evolution of temperature follows $T_f = T_i(\tau_i/\tau_f)^{1/3}$, where T_i and τ_i are the initial temperature and proper time, respectively [41, 42], and T_f and τ_f denote the final temperature and time, respectively. In the case of taking $T_i = 300$ MeV and $\tau_i = 1$ fm [42], we have the chemical freeze-out happens at $\tau_{ch} \approx 6.6$ fm and the kinetic freeze-out happens at

$\tau_0 \approx 15.6$ fm. In the case of considering peripheral collisions, the kinetic freeze-out happens at $T_0 \approx 105$ MeV and $\tau_0 \approx 23.3$ fm. If we consider a non-ideal fluid, for instance, if the viscosity to entropy density ratio η/s is taken to be 0.2, the time delay for the two freeze-outs is slight, comparing with the ideal fluid.

We would like to summarize the main contributions of the present work. Before the reconsideration for the first two models, using a nearly zero β_T in them, the four models do not show similar result. After the reconsideration for the first two models, using a non-zero β_T in them, the four models show similar result. From the comparison with central nuclear collisions, proton-proton collisions are found to be closer to peripheral nuclear collisions, especially in terms of T_0 and β_T . T_0 (β_T) in central collisions is comparable with that in peripheral collisions, and T_0 (β_T) in collisions at the LHC is comparable with that at the RHIC. At any rate, T_0 (β_T) in central collisions is not smaller than that in peripheral collisions, and T_0 (β_T) at the LHC is not smaller than that at the RHIC.

Before giving conclusions, we would like to emphasize that the comparisons of different models and the extractions of T_0 and β_T in small collision system presented in the present work are significative and useful due to collective expansion in small system [43]. This also renders that a large β_T ($\sim 0.4c$) is applied in peripheral nuclear collisions and pp collisions. As we know, some models [6–8, 44–52] are used to extract T_0 and β_T , they are hard to give similar results to others [53–59] in the tendency of quantities. Although the present work gives similar results to [53–59] by the four models, we would like to propose the first and third models due to their use of the Boltzmann distribution which is closer to the well-known ideal gas model. In addition, the hard component has no contribution to T_0 and β_T due to its non-thermal production. Instead, the very-soft and soft components which contribute by the square in the very-low and low p_T regions are used to extract T_0 and β_T . So, the third and fourth fits are applicable, because they work for massive particles and in very-low and low p_T ranges.

In addition, as a complex physics process, high energy collisions contain abundant information. These information include, but are not limited to, electromagnetic field effects [60], strong magnetic field effects [61], particular effects of strangeness [62], etc. These effects may influence the extractions of T_0 and β_T , and then the search for the QCD critical point [63]. As a study at the exploratory stage of development, the present work

still has large space to be improved as accurately as possible. We are interested in the further study on the accurate extractions of T_0 and β_T . Meanwhile, we are interested in the accurate extractions of other types of temperatures such as the effective temperature, chemical freeze-out temperature, and initial temperature, and the comparisons of their dependences on centrality and collision energy.

4 Conclusion

To conclude, the transverse momentum distributions of π^+ , π^- , K^+ , K^- , p , and \bar{p} produced in pp and d -Au collisions at the RHIC, as well as in pp and p -Pb collisions at the LHC, have been analyzed by four models. The first two models utilize the blast-wave model with Boltzmann-Gibbs statistics and with Tsallis statistics, respectively. The last two models perform some linear tendencies in which the Boltzmann and Tsallis distributions are used to extract the effective temperatures, respectively. These models and distributions describe only the contribution of soft excitation process. For the hard scattering process, the inverse power law is uniformly used.

The experimental data measured by the PHENIX, STAR, and ALICE Collaborations are fitted by the model results. We have used a non-zero β_T in the first two methods. The four models present similar results. Both T_0 and β_T in central collisions are comparable with those in peripheral collisions. With the increase of collision energy from the RHIC to LHC, the considered quantities do not decrease in general. Comparing with central nuclear collisions, pp collisions are closer to peripheral nuclear collisions. In nuclear collisions, the excitation degree at the kinetic freeze-out is mainly determined by the heaviest nucleus and collision energy.

Conflicts of Interest

The authors declare that there is no conflict of interests regarding the publication of this paper.

Acknowledgments

Communications from Muhammad Waqas are highly acknowledged. This work was supported by the National Natural Science Foundation of China under Grant Nos. 11575103 and 11747319, the Shanxi Provincial Natural Science Foundation under Grant No. 201701D121005, the Fund for Shanxi “1331 Project” Key Subjects Construction, and the US DOE under contract DE-FG02-87ER40331.A008.

References

- [1] J. Cleymans, H. Oeschler, K. Redlich, S. Wheaton, Comparison of chemical freeze-out criteria in heavy-ion collisions. *Phys. Rev. C* **73**, 034905 (2006). <https://doi.org/10.1103/PhysRevC.73.034905>
- [2] A. Andronic, P. Braun-Munzinger, J. Stachel, Hadron production in central nucleus-nucleus collisions at chemical freeze-out. *Nucl. Phys. A* **772**, 167 (2006). <https://doi.org/10.1016/j.nuclphysa.2006.03.012>
- [3] A. Andronic, P. Braun-Munzinger, J. Stachel, Thermal hadron production in relativistic nuclear collisions. *Acta Phys. Pol. B* **40**, 1005 (2009). There is no doi for this publication. arXiv:0901.2909 [nucl-th]
- [4] A. Andronic, P. Braun-Munzinger, J. Stachel, The horn, the hadron mass spectrum and the QCD phase diagram—the statistical model of hadron production in central nucleus-nucleus collisions. *Nucl. Phys. A* **834**, 237c (2010). <https://doi.org/10.1016/j.nuclphysa.2009.12.048>
- [5] S. Chatterjee, S. Das, L. Kumar, D. Mishra, B. Mohanty, R. Sahoo, N. Sharma, Freeze-out parameters in heavy-ion collisions at AGS, SPS, RHIC, and LHC Energies. *Adv. High Energy Phys.* **2015**, 349013 (2015). <https://doi.org/10.1155/2015/349013>
- [6] E. Schnedermann, J. Sollfrank, U. Heinz, Thermal phenomenology of hadrons from 200A GeV S+S collisions. *Phys. Rev. C* **48**, 2462 (1993). <https://doi.org/10.1103/PhysRevC.48.2462>
- [7] B.I. Abelev et al., (STAR Collaboration), Systematic measurements of identified particle spectra in pp, d+Au, and Au+Au collisions at the STAR detector. *Phys. Rev. C* **79**, 034909 (2009). <https://doi.org/10.1103/PhysRevC.79.034909>
- [8] B.I. Abelev et al., (STAR Collaboration), Identified particle production, azimuthal anisotropy, and interferometry measurements in Au+Au collisions at $\sqrt{s_{NN}} = 9.2$ GeV. *Phys. Rev. C* **81**, 024911 (2010). <https://doi.org/10.1103/PhysRevC.81.024911>
- [9] Z.B. Tang, Y.C. Xu, L.J. Ruan, G. van Buren, F.Q. Wang, Z.B. Xu, Spectra and radial flow in relativistic heavy ion collisions with Tsallis statistics in a blast-wave description. *Phys. Rev. C* **79**, 051901(R) (2009). <https://doi.org/10.1103/PhysRevC.79.051901>
- [10] S. Takeuchi, K. Murase, T. Hirano, P. Huovinen, Y. Nara, Effects of hadronic rescattering on multistrange hadrons in high-energy nuclear collisions. *Phys. Rev. C* **92**, 044907 (2015). <https://doi.org/10.1103/PhysRevC.92.044907>
- [11] H. Heiselberg, A.M. Levy, Elliptic flow and Hanbury-Brown-Twiss in noncentral nuclear collisions. *Phys. Rev. C* **59**, 2716 (1999). <https://doi.org/10.1103/PhysRevC.59.2716>
- [12] U.W. Heinz, Lecture Notes for Lectures Presented at the 2nd CERN–Latin-American School of High-Energy Physics, June 1–14, 2003, San Miguel Regla, Mexico (2004). arXiv:hep-ph/0407360
- [13] R. Russo, Measurement of D^+ meson production in p-Pb collisions with the ALICE detector, Ph.D. Thesis, Universita degli Studi di Torino, Italy (2015). arXiv:1511.04380 [nucl-ex]
- [14] H.-L. Lao, F.-H. Liu, B.-C. Li, M.-Y. Duan, Kinetic freeze-out temperatures in central and peripheral collisions: Which one is larger? *Nucl. Sci. Tech.* **29**, 82 (2018). <https://doi.org/10.1007/s41365-018-0425-x>
- [15] H.-R. Wei, F.-H. Liu, R.A. Lacey, Kinetic freeze-out temperature and flow velocity extracted from transverse momentum spectra of final-state light flavor particles produced in collisions at RHIC and LHC. *Eur. Phys. J. A* **52**, 102 (2016). <https://doi.org/10.1140/epja/i2016-16102-6>
- [16] H.-L. Lao, H.-R. Wei, F.-H. Liu, R.A. Lacey, An evidence of mass-dependent differential kinetic freeze-out scenario observed in Pb-Pb collisions at 2.76 TeV. *Eur. Phys. J. A* **52**, 203 (2016). <https://doi.org/10.1140/epja/i2016-16203-2>
- [17] H.-R. Wei, F.-H. Liu, R.A. Lacey, Disentangling random thermal motion of particles and collective expansion of source from transverse momentum spectra in high energy collisions. *J. Phys. G* **43**, 125102 (2016). <https://doi.org/10.1088/0954-3899/43/12/125102>
- [18] J. Cleymans, D. Worku, Relativistic thermodynamics: Transverse momentum distributions in high-energy physics. *Eur. Phys. J. A* **48**, 160 (2012). <https://doi.org/10.1140/epja/i2012-12160-0>
- [19] H. Zheng, L.L. Zhu, Comparing the Tsallis distribution with and without thermodynamical description in p+p collisions. *Adv. High Energy Phys.* **2016**, 9632126 (2016). <https://doi.org/10.1155/2016/9632126>
- [20] A. Adare et al., (PHENIX Collaboration), Spectra and ratios of identified particles in Au+Au and d+Au collisions at $\sqrt{s_{NN}} = 200$ GeV. *Phys. Rev. C* **88**, 024906 (2013). <https://doi.org/10.1103/PhysRevC.88.024906>
- [21] J. Adams et al., (STAR Collaboration), Identified hadron spectra at large transverse momentum in p+p and d+Au collisions at $\sqrt{s_{NN}} = 200$ GeV. *Phys. Lett. B* **637**, 161 (2006). <https://doi.org/10.1016/j.physletb.2006.04.032>
- [22] G. Agakishiev et al., (STAR Collaboration), Identified hadron compositions in p+p and Au+Au collisions at high transverse momenta at $\sqrt{s_{NN}} = 200$ GeV. *Phys. Rev. Lett.* **108**, 072302 (2012). <https://doi.org/10.1103/PhysRevLett.108.072302>
- [23] J. Adams et al., (STAR Collaboration), Pion, kaon, proton and anti-proton transverse momentum distributions from p+p and d+Au collisions at $\sqrt{s_{NN}} = 200$ GeV. *Phys. Lett. B* **616**, 8 (2005). <https://doi.org/10.1016/j.physletb.2005.04.041>

- [24] J. Adam et al., (ALICE Collaboration), Multiplicity dependence of charged pion, kaon, and (anti)proton production at large transverse momentum in p-Pb collisions at $\sqrt{s_{NN}} = 5.02$ TeV. *Phys. Lett. B* **760**, 720 (2016). <https://doi.org/10.1016/j.physletb.2016.07.050>
- [25] B. Abelev et al., (ALICE Collaboration), Production of charged pions, kaons and protons at large transverse momenta in pp and Pb-Pb collisions at $\sqrt{s_{NN}} = 2.76$ TeV. *Phys. Lett. B* **736**, 196 (2014). <https://doi.org/10.1016/j.physletb.2014.07.011>
- [26] R. Odorico, Does a transverse energy trigger actually trigger on large- p_T jets? *Phys. Lett. B* **118**, 151 (1982). [https://doi.org/10.1016/0370-2693\(82\)90620-7](https://doi.org/10.1016/0370-2693(82)90620-7)
- [27] G. Arnison et al., (UA1 Collaboration), Transverse momentum spectra for charged particles at the CERN proton-antiproton collider. *Phys. Lett. B* **118**, 167 (1982). [https://doi.org/10.1016/0370-2693\(82\)90623-2](https://doi.org/10.1016/0370-2693(82)90623-2)
- [28] T. Mizoguchi, M. Biyajima, N. Suzuki, Analyses of whole transverse momentum distributions in $p\bar{p}$ and pp collisions by using a modified version of Hagedorn's formula. *Int. J. Mod. Phys. A* **32**, 1750057 (2017). <https://doi.org/10.1142/S0217751X17500579>
- [29] http://www.phenix.bnl.gov/WWW/show_plot.php.html, quoted from ref. [19] (which shows the web page) in P. Guptaroy, G. Sau, S.K. Biswas, S. Bhattacharyya, Understanding the characteristics of multiple production of light hadrons in Cu+Cu interactions at various RHIC energies: A model-based analysis. *Nuovo Cimento B* **125**, 1071 (2010). <https://doi.org/10.1393/ncb/i2010-10913-4>, arXiv:0907.2008v2 [hep-ph]
- [30] B.I. Abelev et al., (STAR Collaboration), Spectra of identified high- p_T π^\pm and $p(\bar{p})$ in Cu+Cu collisions at $\sqrt{s_{NN}} = 200$ GeV. *Phys. Rev. C* **81**, 054907 (2010). <https://doi.org/10.1103/PhysRevC.81.054907>
- [31] E.K.G. Sarkisyan, A.S. Sakharov, Multihadron production features in different reactions. *AIP Conf. Proc.* **828**, 35 (2006). <https://doi.org/10.1063/1.2197392>
- [32] E.K.G. Sarkisyan, A.S. Sakharov, Relating multihadron production in hadronic and nuclear collisions. *Eur. Phys. J. C* **70**, 533 (2010). <https://doi.org/10.1140/epjc/s10052-010-1493-1>
- [33] A.N. Mishra, R. Sahoo, E.K.G. Sarkisyan, A.S. Sakharov, Effective-energy budget in multiparticle production in nuclear collisions. *Eur. Phys. J. C* **74**, 3147 (2014). <https://doi.org/10.1140/epjc/s10052-015-3275-2>; and Erratum. *Eur. Phys. J. C* **75**, 70 (2015). <https://doi.org/10.1140/epjc/s10052-014-3147-1>
- [34] E.K.G. Sarkisyan, A.N. Mishra, R. Sahoo, A.S. Sakharov, Multihadron production dynamics exploring the energy balance in hadronic and nuclear collisions. *Phys. Rev. D* **93**, 054046 (2016). <https://doi.org/10.1103/PhysRevD.93.054046>; and Addendum. *Phys. Rev. D* **93**, 079904 (2016). <https://doi.org/10.1103/PhysRevD.93.079904>
- [35] E.K.G. Sarkisyan, A.N. Mishra, R. Sahoo, A.S. Sakharov, Centrality dependence of midrapidity density from GeV to TeV heavy-ion collisions in the effective-energy universality picture of hadroproduction. *Phys. Rev. D* **94**, 011501(R) (2016). <https://doi.org/10.1103/PhysRevD.94.011501>
- [36] C. Patrignani et al., (Particle Data Group), Review of particle physics. *Chin. Phys. C* **40**, 100001 (2016). <https://doi.org/10.1088/1674-1137/40/10/100001>
- [37] F.-H. Liu, Y.-Q. Gao, B.-C. Li, Comparing two-Boltzmann distribution and Tsallis statistics of particle transverse momenta in collisions at LHC energies. *Eur. Phys. J. A* **50**, 123 (2014). <https://doi.org/10.1140/epja/i2014-14123-9>
- [38] A.N. Tawfik, Axiomatic nonextensive statistics at NICA energies. *Eur. Phys. J. A* **52**, 253 (2016). <https://doi.org/10.1140/epja/i2016-16253-4>
- [39] A.N. Tawfik, H. Yassin, E.R.A. Elyazeed, On thermodynamic self-consistency of generic axiomatic-nonextensive statistics. *Chin. Phys. C* **41**, 053107 (2017). <https://doi.org/10.1088/1674-1137/41/5/053107>
- [40] A.N. Tawfik, Lattice QCD thermodynamics and RHIC-BES particle production within generic nonextensive statistics. *Phys. Part. Nucl. Lett. (PEPAN)* **15**, 199 (2018). <https://doi.org/10.1134/S1547477118030196>
- [41] J.D. Bjorken, Highly relativistic nucleus-nucleus collisions: The central rapidity region. *Phys. Rev. D* **27**, 140 (1983). <https://doi.org/10.1103/PhysRevD.27.140>
- [42] K. Okamoto, C. Nonaka, A new relativistic viscous hydrodynamics code and its application to the Kelvin-Helmholtz instability in high-energy heavy-ion collisions. *Eur. Phys. J. C* **77**, 383 (2017). <https://doi.org/10.1140/epjc/s10052-017-4944-0>
- [43] H.C. Song, Y. Zhou, K. Gajdošová, Collective flow and hydrodynamics in large and small systems at the LHC. *Nucl. Sci. Tech.* **28**, 99 (2017). <https://doi.org/10.1007/s41365-017-0245-4>
- [44] S. Das, (for the STAR Collaboration), Identified particle production and freeze-out properties in heavy-ion collisions at RHIC Beam Energy Scan program. *EPJ Web of Conf.* **90**, 08007 (2015). <https://doi.org/10.1051/epjconf/20159008007>
- [45] S. Das, (for the STAR Collaboration), Centrality dependence of freeze-out parameters from the beam energy scan at STAR. *Nucl. Phys. A* **904–905**, 891c (2013). <https://doi.org/10.1016/j.nuclphysa.2013.02.158>
- [46] L. Adamczyk et al., (STAR Collaboration), Bulk properties of the medium produced in relativistic heavy-ion collisions from the beam energy scan program. *Phys. Rev. C* **96**, 044904 (2017). <https://doi.org/10.1103/PhysRevC.96.044904>
- [47] X.F. Luo, Exploring the QCD phase structure with beam energy scan in heavy-ion

- collisions. Nucl. Phys. A **956**, 75 (2016). <https://doi.org/10.1016/j.nuclphysa.2016.03.025>
- [48] C. Markert, (for the STAR Collaboration), Resonance production in heavy-ion collisions at STAR. J. Phys. G **35**, 044029 (2008). <https://doi.org/10.1088/0954-3899/35/4/044029>
- [49] I. Melo, B. Tomášik, Reconstructing the final state of Pb+Pb collisions at $\sqrt{s_{NN}} = 2.76$ TeV. J. Phys. G **43**, 015102 (2016). <https://doi.org/10.1088/0954-3899/43/1/015102>
- [50] A. Iordanova, (for the STAR Collaboration), Strangeness and bulk freeze-out properties at RHIC. J. Phys. G **35**, 044008 (2008). <https://doi.org/10.1088/0954-3899/35/4/044008>
- [51] A. Iordanova, (for the STAR Collaboration), O. Baranikova, R. Hollis, System size dependence of freeze-out properties at RHIC. Int. J. Mod. Phys. E **16**, 1800 (2007). <https://doi.org/10.1142/S0218301307007027>
- [52] A. Ortiz, G. Bencédi, H. Bello, Revealing the source of the radial flow patterns in proton-proton collisions using hard probes. J. Phys. G **44**, 065001 (2017). <https://doi.org/10.1088/1361-6471/aa6594>
- [53] S.S. Adler et al, (PHENIX Collaboration), Identified charged particle spectra and yields in Au+Au collisions at $\sqrt{s_{NN}} = 200$ GeV. Phys. Rev. C **69**, 034909 (2004). <https://doi.org/10.1103/PhysRevC.69.034909>
- [54] S. Chatterjee, B. Mohanty, R. Singh, Freezeout hypersurface at energies available at the CERN Large Hadron Collider from particle spectra: Flavor and centrality dependence. Phys. Rev. C **92**, 024917 (2015). <https://doi.org/10.1103/PhysRevC.92.024917>
- [55] Z.B. Tang, L. Yi, L.J. Ruan, M. Shao, H.F. Chen, C. Li, B. Mohanty, P. Sorensen, A.H. Tang, Z.B. Xu, The statistical origin of constituent-quark scaling in the QGP hadronization. Chin. Phys. Lett. **30**, 031201 (2013). <https://doi.org/10.1088/0256-307X/30/3/031201>
- [56] K. Jiang, Y.Y. Zhu, W.T. Liu, H.F. Chen, C. Li, L.J. Ruan, Z.B. Tang, Z.B. Xu, Onset of radial flow in p+p collisions. Phys. Rev. C **91**, 024910 (2015). <https://doi.org/10.1103/PhysRevC.91.024910>
- [57] B. De, Non-extensive statistics and understanding particle production and kinetic freeze-out process from p_T -spectra at 2.76 TeV. Eur. Phys. J. A **50**, 138 (2014). <https://doi.org/10.1140/epja/i2014-14138-2>
- [58] D. Thakur, S. Tripathy, P. Garg, R. Sahoo, J. Cleymans, Proceedings of the 11th Workshop on Particle Correlations and Femtoscopy (WPCF 2015), Nov. 3–7 2015, Warsaw, Poland (2016). arXiv:1603.04971 [hep-ph]
- [59] D. Thakur, S. Tripathy, P. Garg, R. Sahoo, J. Cleymans, Indication of a differential freeze-out in proton-proton and heavy-ion collisions at RHIC and LHC energies. Adv. High Energy Phys. **2016**, 4149352 (2016). <https://doi.org/10.1155/2016/4149352>
- [60] X.-G. Deng, Y.-G. Ma, Electromagnetic field effects on nucleon transverse momentum for heavy ion collisions around 100 A MeV. Nucl. Sci. Tech. **28**, 182 (2017). <https://doi.org/10.1007/s41365-017-0337-1>
- [61] K. Hattori, X.-G. Huang, Novel quantum phenomena induced by strong magnetic fields in heavy-ion collisions. Nucl. Sci. Tech. **28**, 26 (2017). <https://doi.org/10.1007/s41365-016-0178-3>
- [62] W.-Z. Jiang, R.-Y. Yang, S.-N. Wei, Strangeness to increase the density of finite nuclear systems in constraining the high-density nuclear equation of state. Nucl. Sci. Tech. **28**, 180 (2017). <https://doi.org/10.1007/s41365-017-0333-5>
- [63] X.-F. Luo, N. Xu, Search for the QCD critical point with fluctuations of conserved quantities in relativistic heavy-ion collisions at RHIC: An overview. Nucl. Sci. Tech. **28**, 112 (2017). <https://doi.org/10.1007/s41365-017-0257-0>